PL-TR-95-2059

PLASMASPHERIC MODELING STUDIES, SUBSTORM RESPONSE MODELING AND PLANETARY WAVE SIGNATURES

Matthew W. Fox, Xiaoqing Pi and Jeffrey M. Forbes

Boston University Center for Space Physics

725 Commonwealth Avenue

Boston, Massachusetts 02215

June 1995

Scientific Report No. 2

approved for public release; distribution unlimited

PHILLIPS LABORATORY
Directorate of Geophysics
AIR FORCE MATERIEL COMMAND
HANSCOM AFB, MA 01730-3010

"This technical report has been reviewed and is approved for publication"

Frank A. Marcos
FRANK A. MARCOS
Contract Manager

David N. Anderson
DAVID N. ANDERSON
Branch Chief

WILLIAM K. VICKERY
Division Director

This report has been reviewed by the ESC Public Affairs Office (PA) and is releasable to the National Technical Information Service (NTIS).

Qualified requestors may obtain additional copies from the Defense Technical Information Center (DTIC). All others should apply to the National Technical Information Service (NTIS).

If your address has changed, if you wish to be removed from the mailing list, or if the addressee is no longer employed by your organization, please notify PL/TSI, 29 Randolph Road, Hanscom AFB, MA 01731-3010. This will assist us in maintaining a current mailing list.

Do not return copies of this report unless contractual obligations or notices on a specific document requires that it be returned.

REPORT DOCUMENTATION PAGE

Form Approved
OMB No. 0704-0188

1. AGENCY USE ONLY *(Leave blank)*

2. REPORT DATE
June 1995

3. REPORT TYPE AND DATES COVERED
Scientific No. 2

4. TITLE AND SUBTITLE
Plasmaspheric Modeling Studies, Substorm Response Modeling and Planetary Wave Signatures

5. FUNDING NUMBERS
PE 63707F
PR 4026 TA GL WU MA

Contract F19628-93-K-0012

6. AUTHOR(S)
Matthew W. Fox, X. Q. Pi and Jeffrey M. Forbes

7. PERFORMING ORGANIZATION NAME(S) AND ADDRESS(ES)

Boston University
Center for Space Physics
725 Commonwealth Avenue
Boston, MA 02215

8. PERFORMING ORGANIZATION REPORT NUMBER

9. SPONSORING/MONITORING AGENCY NAME(S) AND ADDRESS(ES)

Phillips Laboratory
29 Randolph Road
Hanscom AFB, MA 01731-3010

Contract Manager: Frank Marcos/GPIM

10. SPONSORING/MONITORING AGENCY REPORT NUMBER
PL-TR-95-2059

11. SUPPLEMENTARY NOTES

12a. DISTRIBUTION/AVAILABILITY STATEMENT

Approved for public release;
distribution unlimited

12b. DISTRIBUTION CODE

13. ABSTRACT *(Maximum 200 words)*

A coupled ionosphere-plasmasphere model has been adapted for use as an extension to an ongoing ionospheric specification model. The changes made and their significance are described herein, along with the discussion of the nature of numerical solutions to ions in diffusive equillibrium and the significance of ion-ion coupling. Secondly, dynamical modeling work has been undertaken to investigate the nature of the ionospheric response to substorm activity. Finally, SETA-based measurements of thermospheric density have been analyzed for wavelike structures and responses.

14. SUBJECT TERMS

plasmaspheric modeling, numerical modeling,
ionospheric modeling,
planetary waves

15. NUMBER OF PAGES
54

16. PRICE CODE

17. SECURITY CLASSIFICATION OF REPORT
Unclassified

18. SECURITY CLASSIFICATION OF THIS PAGE
Unclassified

19. SECURITY CLASSIFICATION OF ABSTRACT
Unclassified

20. LIMITATION OF ABSTRACT
SAR

NSN 7540-01-280-5500

Standard Form 298 (Rev. 2-89)
Prescribed by ANSI Std Z39-18
298-102

TABLE OF CONTENTS

Illustrations

Figure 1. A comparison of Nmax values over low latitudes for March equinox, solar moderate conditions derived from four models (a) upper left panel, the GTIM (b) upper right panel, the original Bailey model (c) lower left panel, the PRISM-Bailey/GTIM-solution (d) lower right panel, the PRISM-Bailey/Bailey-solution. Neutral winds and **E x B** drifts are turned off.

Figure 2. As in Figure 1, but with neutral winds and **E x B** drifts turned on.

Figure 3. As in Figure 2, but with the charge exchange reaction between O and H included in the calculations. Significant differences are seen.

Figure 4. A "fieldline" plot of derived O^+ densities at eight selected Local Times. Here, the densities along the L=1.05 fieldline are compressed in latitude to form "profiles" in the southern (negative) and northern (positive) hemispheres. Two model runs are contrasted, the PB-G model for O^+ only (solid line) and the PB-G model for O^+ and H^+ (dotted line).

Figure 5. As in Figure 4, but showing the derived densities of H^+. The horizontal scale is the same as in Figure 4 to highlight the fact that more O^+ is lost due to charge exchange than H^+ that is formed in the existing model formulation.

Figure 6. As in Figure 4, but showing the loss rates (β) of O^+ (solid line) and H^+ (dotted line). The H^+ rate is seen to be much more rapid (by a factor of around 10^3).

Figure 7. As in Figure 4, but showing the derived densities of He^+ from the PB-B model. This is to highlight the asymmetry that arises in the specification owing to an unphysically strong coupling of He^+ to O^+.

Figure 8. A map showing geographic coordinates of observing sites. Asterisk signs represent the 420 km sub-ionospheric point for total electron content (TEC) observations using Faraday rotation measurements of radio beacon signals from geostationary satellites (ATS-3 and SIRIO) viewed from sites near 75°W and 7°E, respectively. Corresponding local times and dip latitudes are UT+0440 and 50°N at Hamilton, UT+0520 and 38°N at Kennedy Space Center, UT+0428 and 28°N at Ramey, and UT-0028 and 35°N at Florence, respectively.

Figure 9. TEC disturbance events on July 29 and 30, 1982, at four middle and lower latitude sites in the longitudes of near 75°W (Hamilton, KSC, and Ramey) and 7°E (Florence, Italy) are plotted with auroral electrojet (AU/AL, top) and ring current (Dst, bottom) indices. One TEC unit in the figure represents 10^{16} el m^{-2}. Shaded areas indicate ± one standard deviation of 31 day TEC average values centered at the day of July 30. Filled circles indicate the local noon at the four sites. Magnetic daily index (Ap) values are also shown above the top panel.

Figure 10. Ionospheric model results for electrodynamical candidate processes operating during substorms. Panel (*a*) and (*f*) show the substorm activity context specified by auroral AU/AL and ring current Dst indices, respectively. Simulation results are given for the event on July 30, 1982, at one site in the European longitude (Florence, (*b*)) and two sites in the American longitude (KSC (*c*) and Ramey (*d*)). The required electric field perturbations (positive for eastward) for the three sites are also shown in (*e*). The vertical

dotted lines separate periods of expanding and subsided substorm activities. The filled circles give local noon at each site.

Figure 11. Ionospheric results for thermospheric candidate processes operating during substorms. The simulation of the TEC disturbance events on July 30, 1982, at (*b*) Florence, (*c*) KSC, and (*d*) Ramey, using (*e*) thermospheric meridional wind disturbances (positive for poleward) in place of the electric fields used in Figure 6; substorm signatures are given in (*a*) auroral electrojet AU/AL and (*f*) ring current Dst indices. The vertical dotted lines separate periods of expanding and subsided substorm activity. The filled circles give local noon at each site.

Figure 12. The geomagnetic B_x (in relative values) components measured by the CANOPUS network magnetometers at six auroral zone sites (see text). The substorm activity can be seen during 12-18 UT on October 27 and 00-12 UT on October 28, 1992.

Figure 13. (*a*) The CANOPUS magnetometer data during October 27-28, 1992; (*b*) the maximum electron density of the ionospheric F_2 region, (*c*) the heights of the maximum electron density, and (*d*) TEC integrated from the N_e profiles obtained through incoherent scatter radar measurements at Millstone Hill and and Arecibo.

Figure 14. (*a*) CANOPUS magnetometer data (*a*) during October 27-28, 1992. The zonal electric fields (positive eastward) derived from ISR measurements at Sondre Stromfjord, Millstone Hill and Arecibo are shown in panels (*b*), (*c*) and (*d*), respectively. Also plotted in (*c*) and (*d*) are mean patterns of the electric field under conditions of the equinox, magnetic quiet, high solar activity.

Figure 15. The images of 6300Å emissions recorded by the CEDAR/BU Class-I

Imager at Millstone Hill on October 28, 1992. The north is on the top and the east is on the left of each image, and the Millstone Hill observing site is at the center. The bright features in the far north of Millstone Hill appearing at 0142 UT, 0223 UT, and after 0537 UT are the diffuse aurora. The bright arc below the diffuse aurora is the SAR arc that has southward motions starting at about 0730 UT.

Figure 16. Averaged periodogram of wavelike density structures observed by SETA, for quiet (solid line) and active (dashed line) magnetic orbits.

Figure 17. As in Figure 16, but contrasting periodograms for day (solid line) and night (dashed line) orbits.

Figure 18. The upper panel displays the total mass density trend derived from SETA for the July 1983 period, and the larger response in the summer hemisphere is evident. The lower panel shows geomagnetic activity on the same horizontal scale.

Figure 19. As in Figure 18, but only showing the density trend observed from nightside orbits.

Figure 20. The predicted mass density trend for the July 1983 period using the MSISE90 model. The observed trends are not reporoduced.

Figure 21. The upper panel displays the total mass density trend derived from SETA for the August 1983 period, taken from daytime orbits. The lower panel shows geomagnetic activity on the same horizontal scale.

Figure 22. As for Figure 21, but for the August 1982 period.

PLASMASPHERIC MODELING STUDIES
SUBSTORM RESPONSE MODELING
AND PLANETARY WAVE SIGNATURES

1. PLASMASPHERIC MODELING

The Parameterized Real-time Ionospheric Specification Model (hereafter, PRISM) has been developed over recent years (Daniell et al., 1995) to provide accessible and updateable descriptions of the global ionosphere, by means of parameterizations of theoretical model runs and a set of algorithms that allow the incorporation of any available real-time observations. However, an existing limitation with the model is that it lacks a plasmaspheric specification. That is, the component theoretical models have not included the effects and descriptions of the light ions, H^+ and He^+. Much of the ionospheric work performed this year has involved adapting an existing plasmaspheric model for this purpose (requiring consistency with PRISM) and of studies into the nature of the numerical solutions for the derived ion densities (this latter ensuring the stability and physical reliability of the results).

The model originally described by Bailey and Sellek (1990) and recently updated in Bailey et al. (1993) is well-suited to this study, in that it affords a model plasmaspheric specification with many of the same inputs that are used in the GTIM.

The Bailey model derives densities and ion temperatures by means of numerical solutions to the continuity, momentum and energy equations. The ions considered within the model are O^+, H^+, He^+, N_2^+, O_2^+ and NO^+, with density solutions being sought in turn for each ion in that order (specified along magnetic field lines). The model runs from the same base altitude used in the GTIM and extends to the plasmapause. As the model begins without a plasmasphere, a number of simulated days are required for convergence in the H^+ and He^+ densities (essentially filling the plasmasphere; this can be likened to the refilling of the plasmasphere following a magnetic storm).

With regard to adapting and validating this model for the purposes of the PRISM extension, the following points need to be established.

(1) That the same sets of input are used that have been agreed upon in unifying the various component models of PIM/PRISM. This has a number of components.

- verifying that the reaction rates and cross-sections are the same.

- verifying that the same sets of "fudge factors" are applied to the equations in the same fashion.

- verifying that model inputs, such as the thermosphere come from the same version of the model, and that they are used in the same fashion.

(2) That in the case of an O^+-only ionosphere, the results from the numerical solutions agree as much as possible with those from the GTIM (the model specifying O^+ in PRISM).

(3) That the effects of inclusion of the other ions (pricipally the light ions, H^+ and He^+ are physically consistent within the code and the results can be validated against available observations.

These points are discussed in turn in each of the following three sections. Comparisons of model runs are made for the developmental code, referred to as the PRISM-Bailey (or PB) model, to each of the original Bailey model and the GTIM. The conditions for the comparisons presented herein are March equinox, solar moderate and magnetically quiet conditions, for lonigtude 290°E. Commonly, contour plots of profile summary parameters derived from multi-L-shell runs are used, but also presented here are a number of parameters of interest along the L=1.05 fieldline (this L shell passes through/near the highest values of Nmax seen in the contour plots, and thus is an effective means of monitoring the changes).

1.1 Inputs to the Model

This section contains a list of the changes made to the Bailey code in developing a version (PRISM-Bailey) that is consistent with the GTIM.

Firstly, the following cross-sections have been changed from the Bailey model to the PRISM-Bailey model.

- the O^+-O collision cross-section

- photoionization cross-sections for O

- photoabsorption cross-sections for O, N_2 and O_2.

Secondly, there are a number of fudge factors applied to any theoretical model to provide the numerical solutions with a degree of rigidity. Some of these have also been changed in the development of the PRISM Bailey code.

- changing the critical solar zenith angles that flag twilight and nighttime conditions for consistency with the GTIM

- changing the "diffusion fudge factor", a value added to the neutral O density when deriving ion-neutral collision frequencies; this value effectively sets an upper limit to diffusion of ions along fieldlines

- allowing changes to a bottomside altitude up to which checks are made for unstable solutions (and below which chemical equilibrium is assumed).

It also eventuated that some mathematical expressions for analytically evaluated quantities needed to be changed.

- the expression for the divergence of $V_{||}$

- geometric scale factors for the optical depth calculations

- to avoid numeric underflows, pre- and post-multiplication by factors of 10^{10} was included in deriving optical depths

- the altitude marking the apex of the L-shell being considered was fixed in the manner of the GTIM, to ensure that the locations along the fieldline would be the same and thereby facilitating fieldline-oriented comparisons between models.

It is also important to point out that there is an additional fundamental difference to the Bailey and GTIM solutions, in that the former normalizes the momentum term in the continuity equation to the cross-sectional area of the flux tube. As this is not done in the GTIM model, the equations in the PRISM Bailey code have been reformulated accordingly, although the solution method applied to the revised arrays of coefficients (see the next section) is the same.

Finally, a number of model inputs have been altered in the PRISM Bailey code to ensure consistency with PRISM.

- generalization of the usage of **E x B** drift patterns to allow usage of the same files prepared for the PRISM grid

- replacing the section that determines electron and ion temperatures from the heat balance equations with the simple model (Brace and Theis, 1981) preferred in PRISM

- providing solar flux input that can be used by the Bailey model but that is derived from the Hinteregger et al. (1981) flux model preferred in PRISM

- extending the wavelength range considered to most nearly match that used in the GTIM

- nighttime production is changed to the method used in the GTIM

- secondary O photoionization is changed to the method used in the GTIM

- deriving thermospheric winds from the HWM-87 (Hedin et al., 1988) rather than the HWM-90 (Hedin et al., 1991)

- using an input value of solar flux, rather than one appropriate to a designated epoch

- using the Bailey code with a dipole magnetic field, and a North Pole consistent with the value used in the GTIM.

1.2 The nature of O^+ solutions

Each model under consideration here, the original Bailey, the PRISM Bailey, and the GTIM, derives O^+ density solutions in the same basic manner; that is, by substituting an expression for the momentum equation for that ion into the continuity equations and then expressing the resultant equation in finite-differences. There are, however, some differences between the Bailey and GTIM solutions that need to be discussed here.

The Bailey code determines a solution for the ion density, N_i, with respect to the along-the-fieldline variable q (q=$R_E^2 cos(0)/r^2$, where 0 is the magnetic colatitude), that is fully implicit in nature, with the use of a tridiagonal matrix solution method. In the GTIM, a solution is determined for the variable G, where N = Y. G [Y = $\int^r \frac{mg}{k(T_e+T_i)}$, with the latter being a solution to the diffusion operator so that G becomes constant at high altitudes], with respect to the along-the-fieldline variable X (a transformation of q that is evenly-spaced), and that is of a Crank-Nicholson type, using a recursive solution type. These differences are relevant to the discussion of results that follows.

As it became evident that some differences in derived densities did result from the nature of the solution, two separate versions of the PRISM-Bailey (PB code evolved. The first, PB-Bailey (or PB-B) uses the input parameters described in the previous section for the PRISM Bailey code, but retains the Bailey-like solution type. The second, PB-GTIM (or PB-G) uses the abovementioned inputs but bases the solution on a GTIM-like solution, in which all the same coefficient arrays are formed and the exact same type of solution to the GTIM is sought.

In making comparisons we are therefore looking for the following:

- the differences between the original Bailey code and the GTIM, as they reflect the "before" and "after" results of the PRISM Bailey code

- the differences between the PB-G and GTIM codes, as they reflect the degree to which the PRISM-related changes have not been successfully incorporated

- the differences between the PB-B and PB-G, as they reflect the degree to which the results are sensitive to the type of numerical solution being sought.

Let us begin discussion with Figure 1, wherein contours of Nmax are shown for the four models described above, in the situation where both thermospheric winds and **E x B** drifts are switched off. It should also be stressed here that the original Bailey model results are based on the default Bailey diffusion fudge factor of 10^{14}, rather than the GTIM value of 10^{12}. This is owing to the fact that the numerical results are not stable in the original Bailey code using the lower value. A large degree of agreement between the model results is apparent, both qualitatively and quantitatively.

Compare these results with those in Figure 2, where now the winds and drifts have been activated in a normal (climatological) sense. The agreement between the GTIM and PB-G models is seen to remain intact in the presence of the various transport terms in the equations. The improvement in physical description of the anomaly region over the original Bailey code is also apparent. What is disturbing in the context of the PRISM Bailey code is the difference between the PB-G and PB-B solutions. Although the general trends in Nmax are very similar, there are clear quantitative differences between the two solutions, especially around the post-sunset increase in the equatorial anomaly where Nmax differs by around 30%. This is purely related to the nature of solution, as inputs (i.e., physical conditions) in the two PRISM Bailey versions are identical (indeed, it is this difference that required the generation of PB-G and PB-B models). Investigations are ongoing into the underlying cause of these differences.

1.3 The effects of other ions

In this section, we discuss how the solution for additional ions (here, the light ions) is implemented in the Bailey code, and we give significant attention to the resultant effects on the derived O^+ densities.

To begin with, H^+ is included. This ion density solution is sought in the same tridiagonal matrix fashion to the finite difference version to the continuity equation for H^+. In the Bailey formalism, this solution is sought following the derived solution for the O^+ densities. No iteration to converged densities is sought. The only source for H^+ is through the charge exhange reaction

$$O^+ + \mathrm{H} \leftrightarrow \mathrm{O} + H^+$$

and this reaction also becomes an additional loss term for the O^+ ions.

Around the F2-peak altitude, this additional loss term is quite significant and effects are quite apparent on Nmax values derived when H^+ has been included. Figure 3 presents the solutions derived for Nmax under these circumstances (except for the GTIM that contains no H effects), to be contrasted with the results in Figure 2. However, there is no production of H^+ at these altitudes. This important point is best demonstrated in fieldline plots. Figure 4 presents O^+ densities along the L=1.05 fieldline at eight different Local Times for the PB-G run, both without (solid line) and with (dotted line) inclusion of the H^+ ion. Drops of 20% in the evening Nmax value are seen. Figure 5 shows the production of H^+ on the same horizontal scale and clearly there is very little compared to the loss of O^+. This happens because the solutions to O^+ and H^+ densities are sought sequentially, rather then interdependently, making it possible for ions to be lost from one place without being formed in the other. Specific to O-H charge exchange, it is the loss rates that give rise to this inconsistency. Firstly, the O^+ solution is sought with a loss rate increased by around 20%, and smaller densities result. Then, the H^+ solutions is found, but owing to a very rapid reverse reaction rate, none of it is retained at Nmax altitudes. Figure 6 contrasts the loss rates to O^+ and H^+ respectively, with $\beta(H^+)$ seen to be far greater. Physically, no H^+ will form at 300km, but sequential ion solutions allow the loss of O^+ to occur. A means of accounting for the rapid reverse reaction in the charge exchange loss term for O^+ is currently under development. A simple method would be to scale the rate by exp(-$\beta(H^+).\delta$T), to allow for the amount of H^+ that can effectively be formed over a time step of δT, allowing for a potentially rapid reverse reaction.

The same correction will not be required for the He^+ ion, because no charge exchange with O^+ occurs. Production of He^+ occurs through direct photoionization and so consistency of ion solutions should not be an issue. However, recent observational studies (reported in the 1994 Fall AGU Meeting, in San Fransisco, CA) have demonstrated that He^+ densities can be quite significant and can in winter, nighttime conditions dominate the topside of the ionosphere. Qualitatively, this will also form part of the validation of the PRISM-Bailey model, prior to generating a model plasmaspheric grid. Developmentally, it means that attention must be given to the derived He^+ densities. The original Bailey code, however, demonstrates a degree of coupling between the O^+ and He^+ ions that leads to unphysical asymmetries in the densities of the latter. An example of this, in fieldline domain, is shown in Figure 7, for L=1.50 and a longer run (five simulated days). The asymmetries in the densities are evident and are seen to increase with each simulated day of the model run. These two ions will need to be largely decoupled in order to provide a realistic description of He^+ densities. This could be achieved either by reducing the relevant cross-section or by altering the He ion temperature.

A series of observations designed to support the validation effort of this model topside specification has been instigated at Millstone Hill, MA. Further topside validation can come from the growing database of in-situ densities measured by DMSP satellites orbiting at an altitude of 840km.

2. SUBSTORM MODELING

Ionsopheric modeling diagnostic work has continued on the nature of TEC disturbances measured at two middle and lower latitude sites (Kennedy Space Center, FL and Ramey, PR) in the American longitude (75°W) and one middle latitude site, Florence, Italy (7°E). A map showing the geographical locations of these sites (including the Hamilton site in which TEC data were also obtained and analysed) is given in Figure 8.

A daytime ionospheric disturbance pattern was identified by case analyses, for middle and lower latitudes at both longitudes during substorms. A positive ionospheric TEC response corresponding to substorm expansion periods, then a depletion or negative response as activity subsides. This TEC disturbance pattern can evolve into a diurnal double maxima (DDM) phenomenon (Pi et al., 1993), if sequential, isolated substorms occur during the daytime. Observations show that this basic pattern can occur at longitudes that differ by at least five hours. Figure 9 gives examples of the TEC disturbance patterns at the two longitudes.

The GTIM was used to model background ionospheric conditions first. As one of the model input parameters, the thermospheric neutral wind model, HWM87, was replaced by HWM90 which is based on the measurements using satellites, incoherent scatter radars (ISRs), and Fabry-Perot interferometers (FPIs), and gives altitude dependence of winds (Hedin et al., 1991). With the new wind model, the GTIM gives slightly higher (about $\leq$ 5%) TEC values than those based on the HWM87. For the case of July 1982, the model run with monthly mean conditions gave TEC values higher than the observations at all three sites. The input meridional wind magnitudes were then adjusted to match the monthly mean TEC values. The required wind adjustments were about 50 m/s, poleward during daytime and equatorward during nighttime.

In the model study, longitudinal comparisons were made for the required electric fields and TADs (assumed to be induced by substorms) that might produce the TEC disturbance patterns observed in different local time sectors. The intention was to distinguish possible global characteristics that may exist in either electric fields or TADs.

The GTIM was next run with both wind and electric field adjustments, the goal neing to match the observed TEC variations. It was found that the model was able to simulate the disturbances with both winds and electric fields, and required magnitudes of winds and electric fields were in a reasonable range (about 50 m/s for winds and 1 mV/m for electric fields) that is consistent with observations under active magnetic conditions. Figures 10 and 11 show the results of TEC disturbance simulations and required electric fields and winds at the three sites. The major differences of the modeling between the effects of winds and electric fields were obtained from the modeling work. For instance, the required winds do not show significant local time differences and are thus inconsistent with previous and recent modeling studies of substorm-induced wind disturbances and TADs by others.

The modeling of electrodynamical effects reveals that, within the longitudes investigated here, the amplitudes of the required electric field disturbances appear to be smaller near dawn and dusk than those in other daytime sectors. This is consistent with a simplified dawn-dusk oriented magnetospheric electric field pattern. The latitudinal gradient of the required electric field magnitudes also shows a consistency with the basic penetration and overshielding assumption, in which the magnitudes decrease toward lower latitudes. However, there are also major uncertainties with the electrodynamic mechanism. Chief among these are penetration and overshielding durations that are inconsistent with past modeling results obtained in the work of Spiro et al. (1988). Recent evidence of substorm effects in the middle-latitude ionosphere by Buonsanto and Foster (1993) shows that a single mechanism may not dominate in each substorm event, and a more complete picture of substorm disturbance mechanisms may be drawn if the interplay between magnetospheric electric fields and neutral winds is better understood.

Case-study modeling scenarios implied that perhaps a single mechanism, such as magnetospheric electric field penetration and overshielding effects, or TADs, or disturbance dynamo effects may not be adequate for individual events. Each of these mechanisms may dominate at times and their separation is a difficult problem. A more complete view of the ionospheric response to substorms at middle and lower latitudes awaits further studies that use a mixture of disturbance sources.

A paper entitled

Longitudinal Effects of Ionospheric Responses to Substorms at Middle and Lower Latitudes: A Case Study, by Xiaoqing Pi, Michael Mendillo, Paolo Spalla, and David N. Anderson,

was accepted for publication by Annale Geophysicae.

To examine the results obtained via TEC data analyses and modeling studies, a comprehensive data set was analysed, which was obtained during an experimental campaign coordinated by Xiaoqing Pi, using multi-diagnostic techniques in October 1992. The techniques involved three incoherent scatter radar facilities (Sondre Stromfjord, Millstone Hill and Arecibo) at high to lower latitudes along the American longitude, a FPI and all-sky camera measuring airglow at Millstone Hill, and a magnetometer chain in the auroral zone. During the campaign, substorm activity was observed at both daytime and nighttime on October 27-28, 1992. Figure 12 shows the magnetometer data for B_x measured at six sites in the auroral zone, covering longitudes from 220°E to 265°E. The ionospheric Nmax, Hmax and TEC, showed moderate disturbances during 36 hours of the campaign, which were closely associated with substorm activity at high latitudes. Figure 13 gives these measurements at Millstone Hill and Arecibo, respectively, with the magnetic conditions at high latitudes.

Electric fields and neutral winds were also derived from the plasma motions and temperatures measured at the middle latitudes using the radars and FPI. The electric fields and meridional winds at different latitudes were compared for substorm effects. As shown in Figure 14, eastward electric field perturbations were seen during 14-16 UT on October 27 and 03-07 UT on October 28 at both Millstone Hill and Arecibo when the electric field was enhanced at the high latitude site. These were identified as electric field penetration effects at both day and night when substorms occurred. Westward electric field perturbations were also observed at the two middle latitude sites when substorm activity was enhanced during 07-11 on October 28. At Arecibo, the southward plasma motions drove the neutrals and thus changed the neutral wind directions. This might have happened at Millstone Hill but results were not as clear as those at Arecibo because of the data quality.

At the subauroral site (Millstone Hill), a SAR arc was observed. This SAR arc showed a dynamical behavior in which the arc moved from the north of Millstone Hill to the south when the major substorm occurred on the night of October 28, 1992, and the zonal electric field showed westward perturbations. Figure 15 shows sequential 6300Å images, demonstrating the SAR arc dynamical behavior.

3. PLANETARY WAVE SIGNATURES

3.1 Small-Scale Waves

SETA density measurements (normalized to a nominal altitude of 200 km) were analyzed to delineate characteristics of relatively small-scale waves (horizontal structures of order 150 to 2500 km) in the data. (Note: This analysis is restricted to *in-track (latitudinal)* structures; the analysis of longitudinal structures is addressed in Section 4.3) The spectral analyses were applied to all available orbits (approximately 15 to 18 per day) during 6 days in 1983 and 10 days in 1982, covering a range of geomagnetic conditions.

This project has been completed during the past year, and a journal article written and accepted for publication in the Journal of Geophysical Research:

"Wave Structures in Lower Thermosphere Density from Satellite Electrostatic Triaxial Accelerometer (SETA) Measurements" by J.M. Forbes, F.A. Marcos, and F. Kamalabadi

As a result of this analysis, the lower thermosphere is found to be frequently characterized by wavelike structures corresponding to peak-to-peak density variations of order 10–40%. Orbit by orbit spectral analyses of densities normalized to 200 km altitude were performed, and these are combined together to construct average periodograms for magnetically quiet and active periods. Integration of these curves provides the relative percentage of total density variance attributable to various horizontal scales; for instance, 10% for $\lambda_H < 750$ km and 70% for $1500 < \lambda_H < 2500$ km. As geomagnetic activity increases from quiet ($K_p < 2$) to active ($K_p > 4$) levels, the spectral energy increases by a factor of two for wavelengths in the range 150 - 500 km and by a factor of four at longer wavelengths (1000 – 2500 km). This is illustrated in Figure 16. In part the spectral energy enhancement at the longer wavelengths reflects mesoscale density variations unrelated to wave activity, but "direct" waves generated by auroral activity and which are known to travel long distances probably also make important contributions at these wavelengths. Similarly, a comparison of day vs. night periodograms for all orbits during 1983 are illustrated in Figure 17. This plot illustrates the enhancement in wave activity which occurs at scales shorter than 400 km during the night, whereas the spectral densities at wavelengths longer than 500 km are virtually the same. The magnetic activity enhancement at shorter scales is also significant, especially at low latitudes, since waves with these horizontal wavelengths are not expected on theoretical grounds to propagate very far within the thermosphere away from an auroral source. Moreover, the shorter scale waves regularly occur during geomagnetically quiet times when an auroral source mechanism is unlikely.

3.2 Magnetic Storm Perturbations

SETA-2 and SETA-3 data have been analyzed during the following periods containing significant changes in geomagnetic activity:

(a) July 20-27, 1983

(b) August 2-10, 1983

(c) August 2-9, 1982

(d) September 3-11, 1982

(e) December 4-14, 1983

Various data visualization tools have been developed to depict the temporal, day/night, and latitudinal/seasonal trends characterizing the response of thermospheric mass density to changes in high-latitude heating during magnetically active periods. Data between 170 and 240 km are normalized to a constant altitude of 200 km. Sliding 11-rev (about 16 hours) means are applied to the data to remove smaller-scale features, and to serve as a "trend" for delineation of the residual densities (see following section).

Figure 18 illustrates the latitude-time variations in total mass density "trend" occurring during the July 1983 period. Note the much larger response occurring in the summer hemisphere; this is due in part to the enhanced Joule heating connected with the larger ionization levels characterizing the summer ionosphere. There is also the tendency for the density perturbation to be carried from summer to winter due to the prevailing thermospheric circulation in that direction. The combination of these two effects gives rise to the large seasonal asymmetry in the density response depicted in Figure 18.

Figure 19 illustrates the SETA density response in the nightside (2230 LST) for the July 1983 period. Note that the density response penetrates much more easily to the equatorial region; this is due to the enhanced equatorward winds which characterize the nighttime thermosphere as opposed to the daytime thermosphere. The corresponding Figure 20 for MSISE90 does not reflect this behavior, pointing to a shortcoming of this empirical model.

Figures 21-24 illustrate the SETA density trends for periods (b), (c), (d), and (e) listed above. Each exhibits the same general response features to the changing magnetic activity levels. In particular, note the enhanced Southern Hemisphere summer response in Figure 24.

A statistical examination was also made regarding the Kp dependence of the densities, in particular the temporal/latitudinal characteristics of this behavior. As illustrated in Figure 25, the higher latitudes correlated best with a Kp delay of 3 hours, wheras the lower latitudes correlated best with a Kp delay of 6 hours. This latitudinal dependence of the time delay is consistent with that required physically for a disturbance to propagating from polar/auroral to low latitudes.

3.3 Longitudinal Wave Structures

By subtracting the measured densities from the "trends", a set of density residuals have been constructed. Figure 26 illustrates the density residuals for the July, 1983 period. Note that throughout this period that longitudinal wave structures with apparent zonal wavenumbers in the range of 2-4 are apparent in the data at about the ±10% level. A "zoom" version of these data is provided in Figure 27. We believe these structures to be a real phenomenon which has not been previously discovered in the thermosphere. We are presently applying various spectral and aliasing techniques to these data to ascertain whether we can unabiguously identify whether these are standing waves (i.e., fixed in longitude) or eastward- or westward-propagating.

When ordered in magnetic coordinates (see Figure 28), these same data exhibit a zonal wavenumber one oscillation which is probably stationary and connected with a magnetic coordinate (UT or longitude) effect. The origin of this feature and its connection to UT/longitude variations in the MSISE90 model are currently under investigation.

4. REFERENCES

Bailey, G. J. and R. Sellek, A mathematical model of the Earth's plasmasphere and its application in a study of He^+ at L=3, *Ann. Geophys*, **8**, 171, 1990

Bailey, G. J., R. Sellek and Y. Rippeth, A modelling study of the equatorial topside ionosphere, *Ann. Geophys*, **11**, 263, 1993

Brace, L. H. and R. F. Theis, Global empirical models of ionospheric electron temperature in the upper F-region and plasmasphere based on in situ measurements from the Atmospheric Explorer-C, ISIS 1 and ISIS 2 satellites, *J. Atmos. Terr. Phys.*, **43**, 1317, 1981.

Buonsanto, M. J., and J. C. Foster, Effects of magnetospheric electric fields and neutral winds on the low-middle latitude ionosphere during the March 20-21, 1990, storm, *J. Geophys. Res., 98*, 19133, 1993.

Daniell, R. E., W. R. Whartenby, L. D. Brown, D. N. Anderson, M. W. Fox, D. T. Decker, P. H. Doherty, J. J. Sojka and R. W. Schunk, "The Parametrized Real-time Ionospheric Specification Model, PRISM", Submitted to Radio Science, 1995.

Hedin, A. E., N. W. Spencer and T. L. Killeen, Empirical global model of upper thermosphere winds based on atmosphere and Dynamics Explorer satellite data, *J. Geophys. Res.*, **93**, 9959, 1988.

Hedin, A. E., M. A. Biondi, R. G. Burnside, G. Hernandez, R. M. Johnson, T. L. Killeen, C. Mazaudier, J. W. Meriwether, J. J. Salah, R. J. Sica, R. W. Smith, N. W.

Sepncer, V. B. Wickwar and T. S. Virdi, Revised global model of thermosphere winds based on satellite and ground-based observations, *J. Geophys. Res.*, **96**, 7657, 1991.

Pi, X., M. Mendillo, M. W. Fox, and D. N. Anderson, Diurnal double maxima patterns in the *F* region ionosphere: Substorm-related aspects, *J. Geophys. Res., 98*, 13677, 1993.

Spiro, R. W., R. A. Wolf, and B. G. Fejer, Penetration of high-latitude-electric-field effects to low latitudes during SUNDIAL 1984, *Ann. Geophysicae, 6*, 39, 1988.

Figure 1

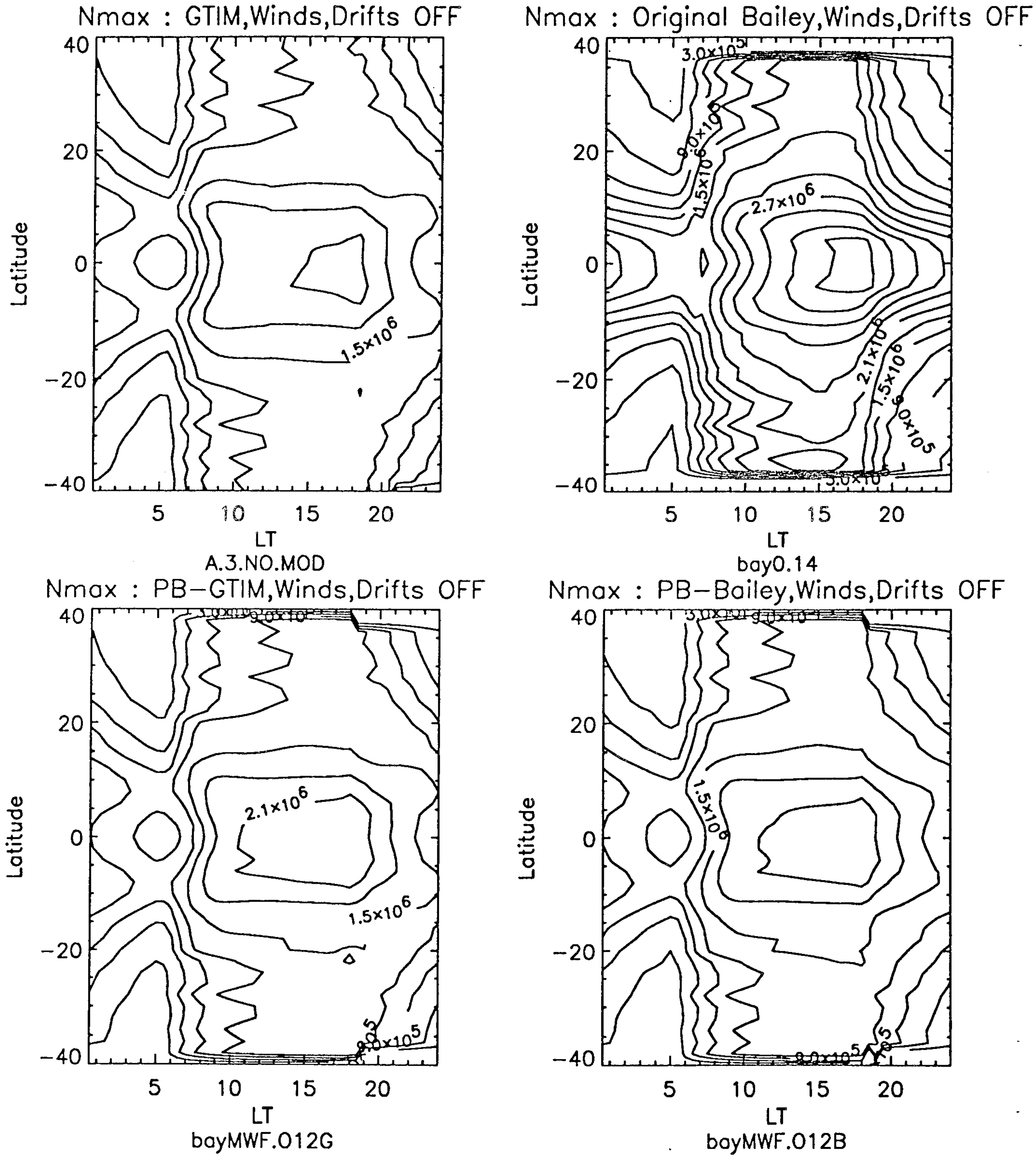

Nmax : GTIM,Winds,Drifts OFF
40
20
0
−20
−40
Latitude
1.5×10^6
5
10
15
20
LT
A.3.NO.MOD
Nmax : Original Bailey,Winds,Drifts OFF
3.0×10^5
9.0×10^5
1.5×10^6
2.7×10^6
2.1×10^6
1.5×10^6
9.0×10^5
3.0×10^5
LT
bay0.14
Nmax : PB−GTIM,Winds,Drifts OFF
2.1×10^6
1.5×10^6
9.0×10^5
LT
bayMWF.012G
Nmax : PB−Bailey,Winds,Drifts OFF
1.5×10^6
9.0×10^5
LT
bayMWF.012B

Figure 2

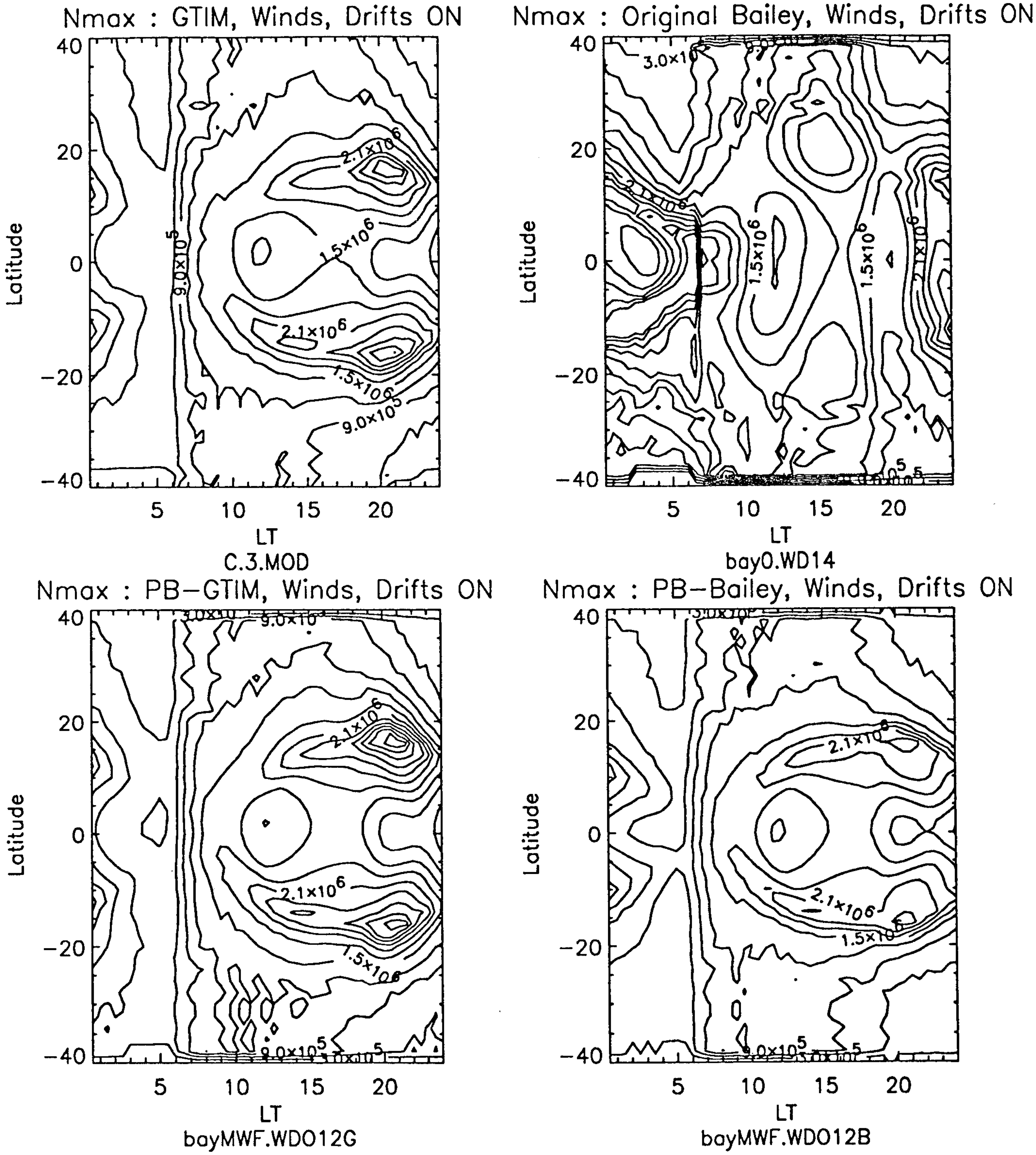
Nmax : GTIM, Winds, Drifts ON

C.3.MOD

Nmax : Original Bailey, Winds, Drifts ON

bay0.WD14

Nmax : PB–GTIM, Winds, Drifts ON

bayMWF.WDO12G

Nmax : PB–Bailey, Winds, Drifts ON

bayMWF.WDO12B

Figure 3

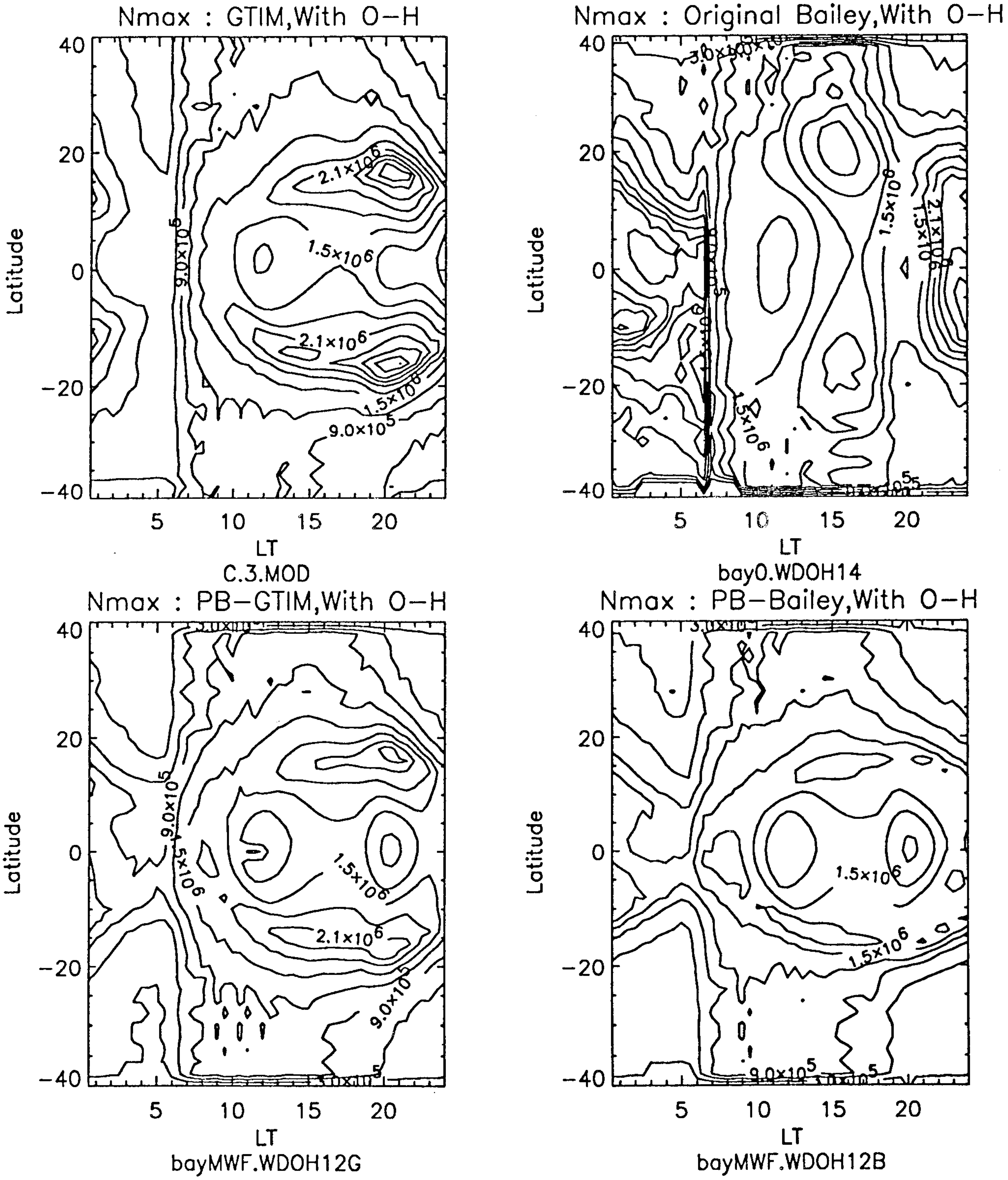

Nmax : GTIM,With O−H
Latitude
40
20
0
−20
−40
5
10
15
20
LT
C.3.MOD
2.1×10⁶
1.5×10⁶
9.0×10⁵
2.1×10⁶
1.5×10⁶
9.0×10⁵
Nmax : Original Bailey,With O−H
Latitude
3.0×10⁵
1.5×10⁶
2.1×10⁶
1.5×10⁶
1.5×10⁶
LT
bay0.WDOH14
Nmax : PB−GTIM,With O−H
Latitude
9.0×10⁵
1.5×10⁶
1.5×10⁶
2.1×10⁶
9.0×10⁵
LT
bayMWF.WDOH12G
Nmax : PB−Bailey,With O−H
Latitude
3.0×10⁵
1.5×10⁶
1.5×10⁶
9.0×10⁵
LT
bayMWF.WDOH12B

Figure 4

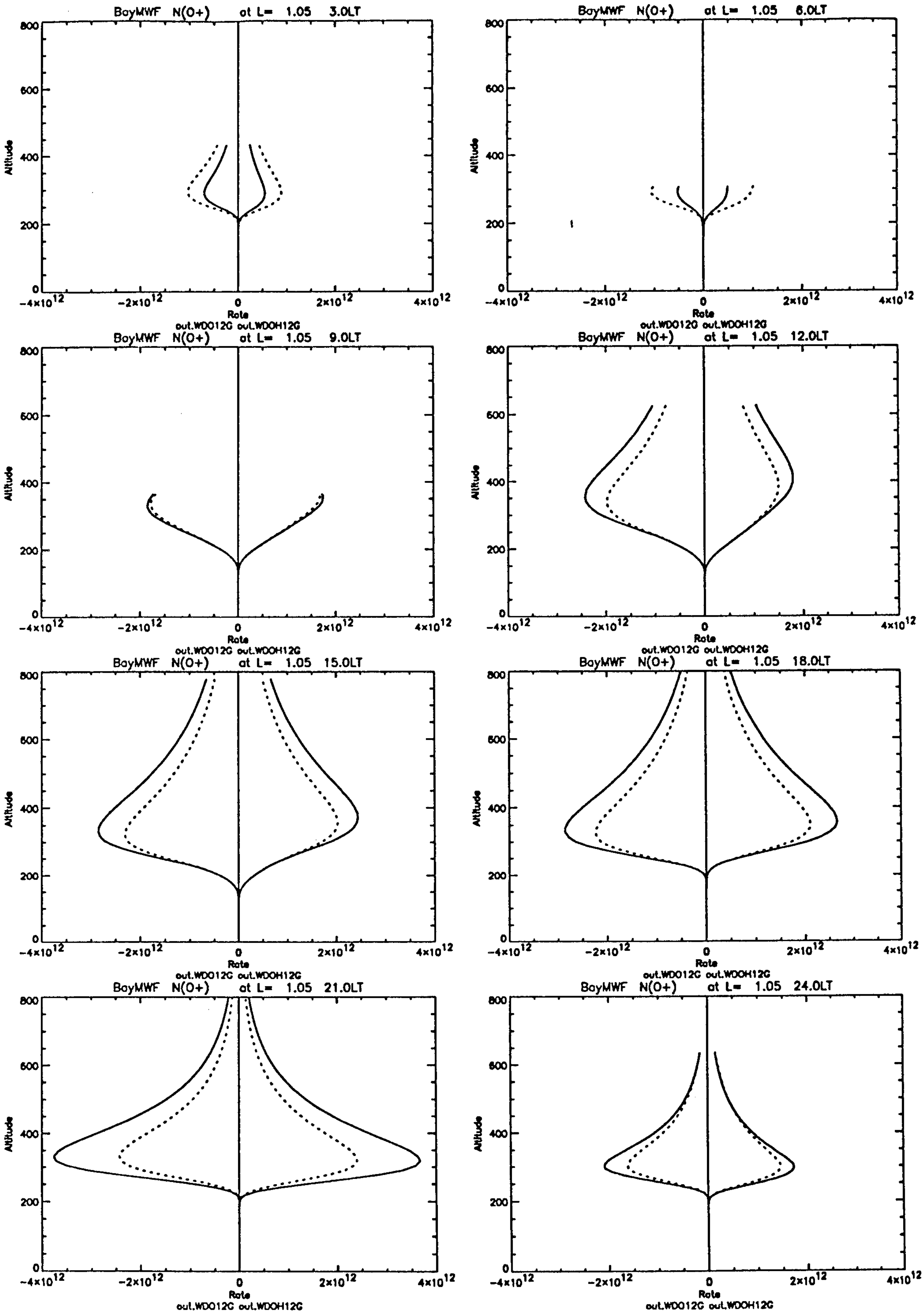
BayMWF N(O+) at L= 1.05 3.0LT
BayMWF N(O+) at L= 1.05 6.0LT
BayMWF N(O+) at L= 1.05 9.0LT
BayMWF N(O+) at L= 1.05 12.0LT
BayMWF N(O+) at L= 1.05 15.0LT
BayMWF N(O+) at L= 1.05 18.0LT
BayMWF N(O+) at L= 1.05 21.0LT
BayMWF N(O+) at L= 1.05 24.0LT
Altitude
0
200
400
600
800
Rate
-4×10^{12}
-2×10^{12}
0
2×10^{12}
4×10^{12}
out.WDO12G out.WDOH12G

Figure 5

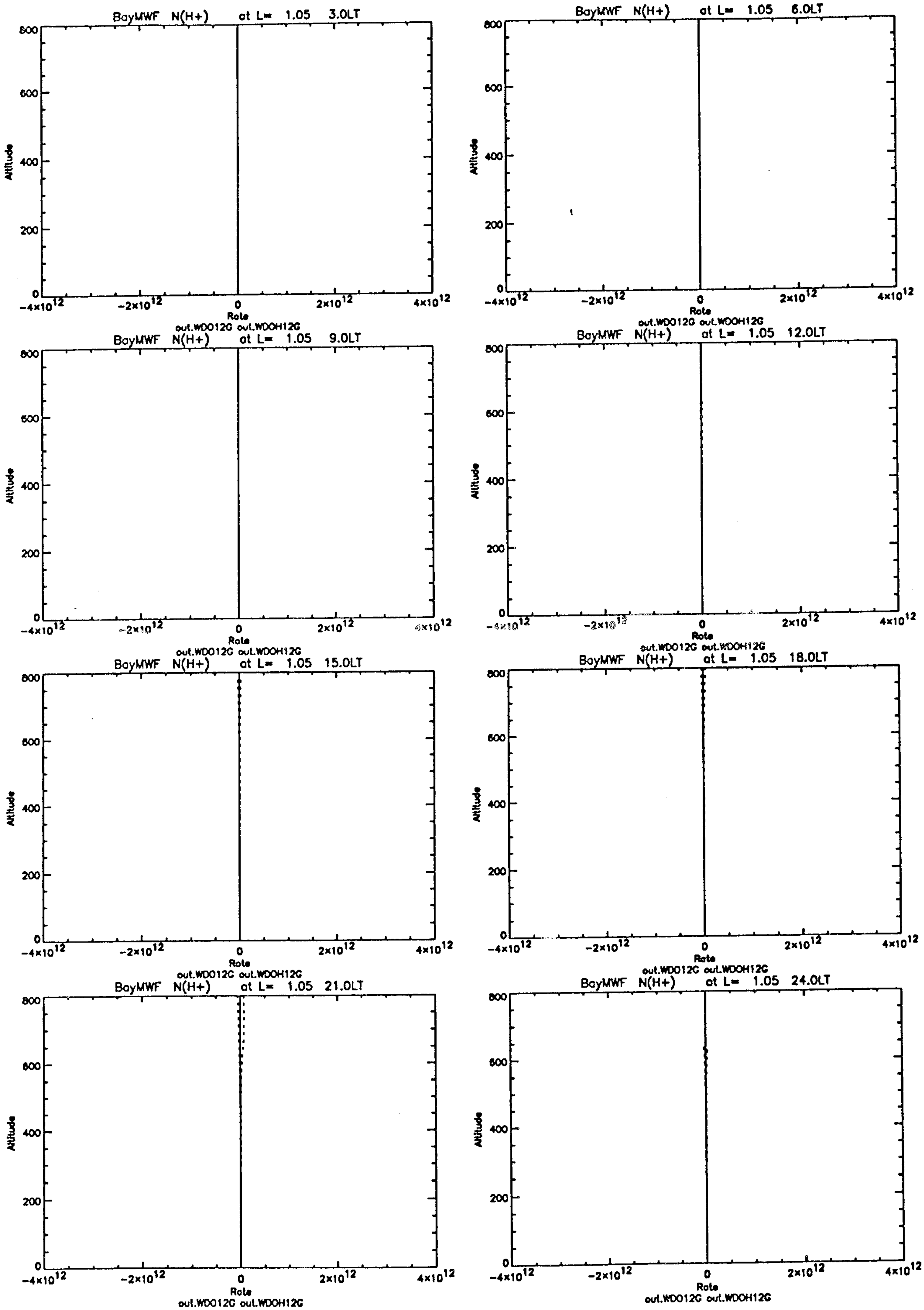
BayMWF N(H+) at L= 1.05 3.0LT
BayMWF N(H+) at L= 1.05 6.0LT
BayMWF N(H+) at L= 1.05 9.0LT
BayMWF N(H+) at L= 1.05 12.0LT
BayMWF N(H+) at L= 1.05 15.0LT
BayMWF N(H+) at L= 1.05 18.0LT
BayMWF N(H+) at L= 1.05 21.0LT
BayMWF N(H+) at L= 1.05 24.0LT
Altitude
0
200
400
600
800
Rate
−4×10^12
−2×10^12
0
2×10^12
4×10^12
out.WDO12G out.WDOH12G

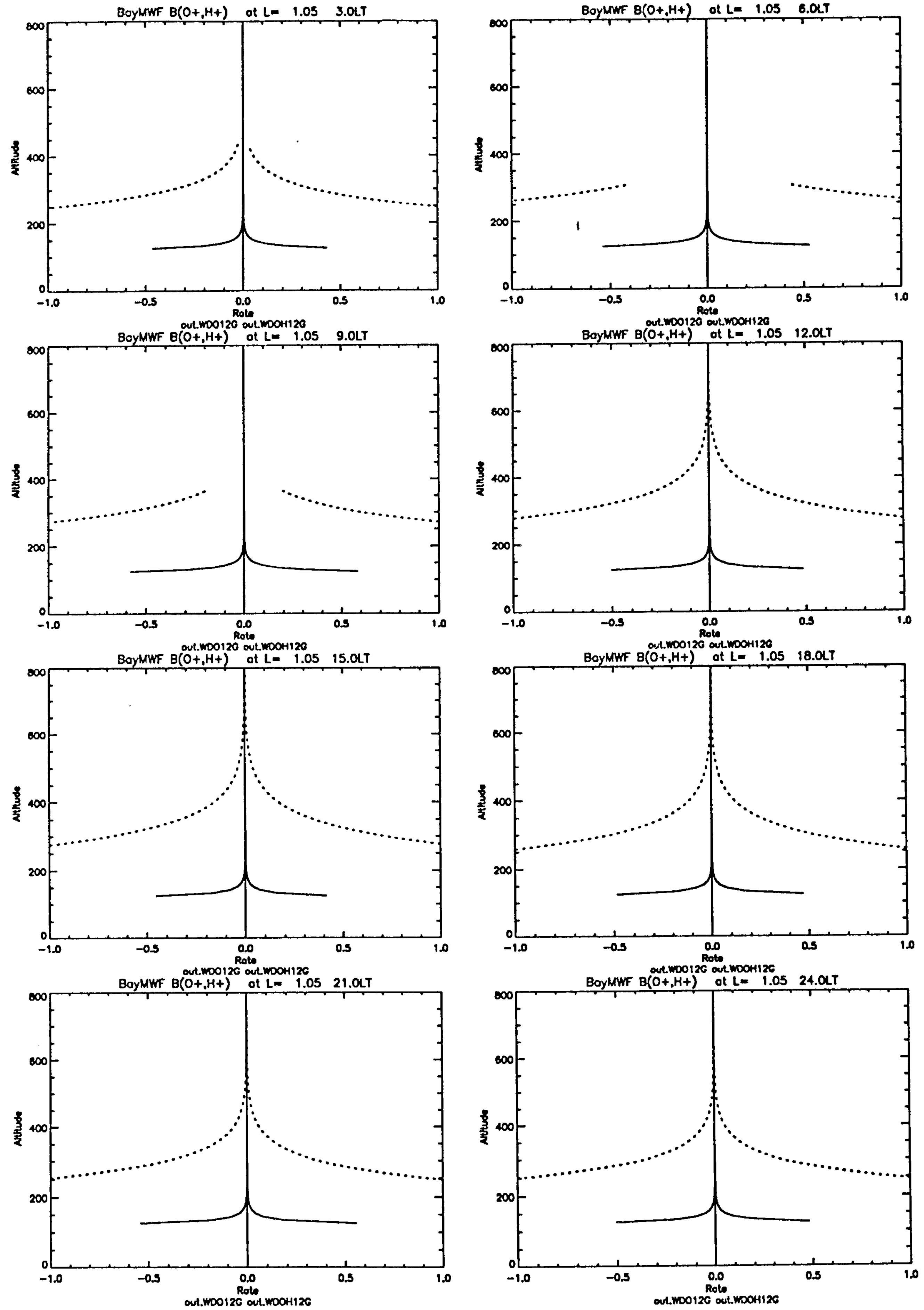
BayMWF B(O+,H+) at L= 1.05 3.0LT
BayMWF B(O+,H+) at L= 1.05 6.0LT
BayMWF B(O+,H+) at L= 1.05 9.0LT
BayMWF B(O+,H+) at L= 1.05 12.0LT
BayMWF B(O+,H+) at L= 1.05 15.0LT
BayMWF B(O+,H+) at L= 1.05 18.0LT
BayMWF B(O+,H+) at L= 1.05 21.0LT
BayMWF B(O+,H+) at L= 1.05 24.0LT
Altitude
800
600
400
200
0
-1.0
-0.5
0.0
0.5
1.0
Rate
out.WDO12G out.WDOH12G

Figure 6

Figure 7

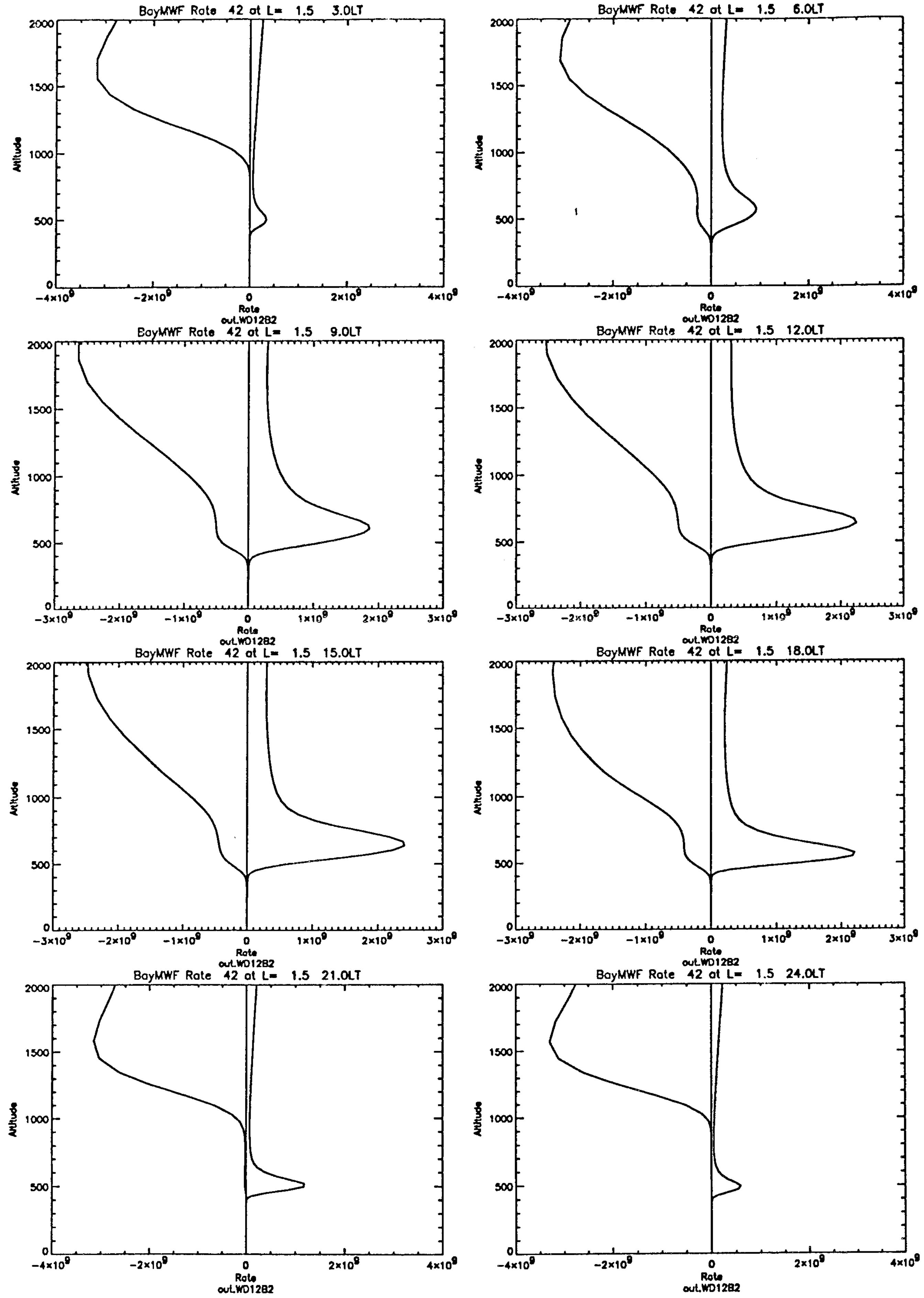

BayMWF Rate 42 at L= 1.5 3.0LT

BayMWF Rate 42 at L= 1.5 6.0LT

BayMWF Rate 42 at L= 1.5 9.0LT

BayMWF Rate 42 at L= 1.5 12.0LT

BayMWF Rate 42 at L= 1.5 15.0LT

BayMWF Rate 42 at L= 1.5 18.0LT

BayMWF Rate 42 at L= 1.5 21.0LT

BayMWF Rate 42 at L= 1.5 24.0LT

Figure 8

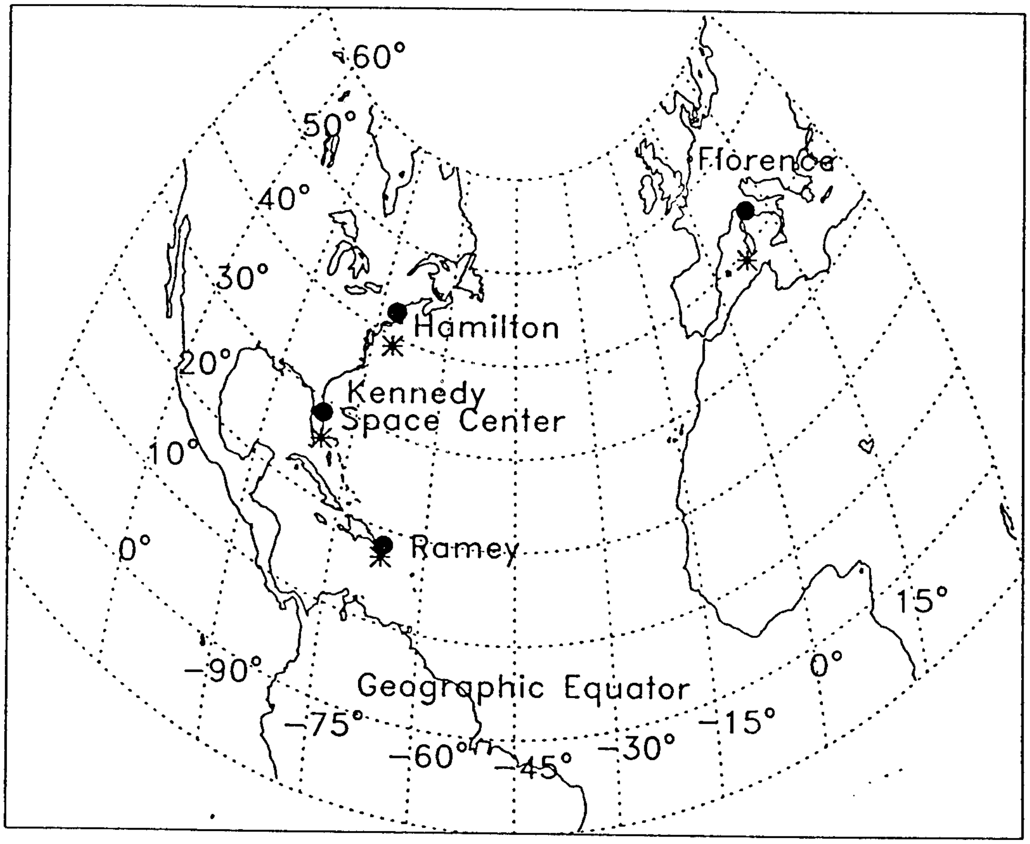
60°
50°
40°
30°
20°
10°
0°
Florence
Hamilton
Kennedy
Space Center
Ramey
15°
0°
−90°
Geographic Equator
−75°
−60°
−45°
−30°
−15°

Figure 9

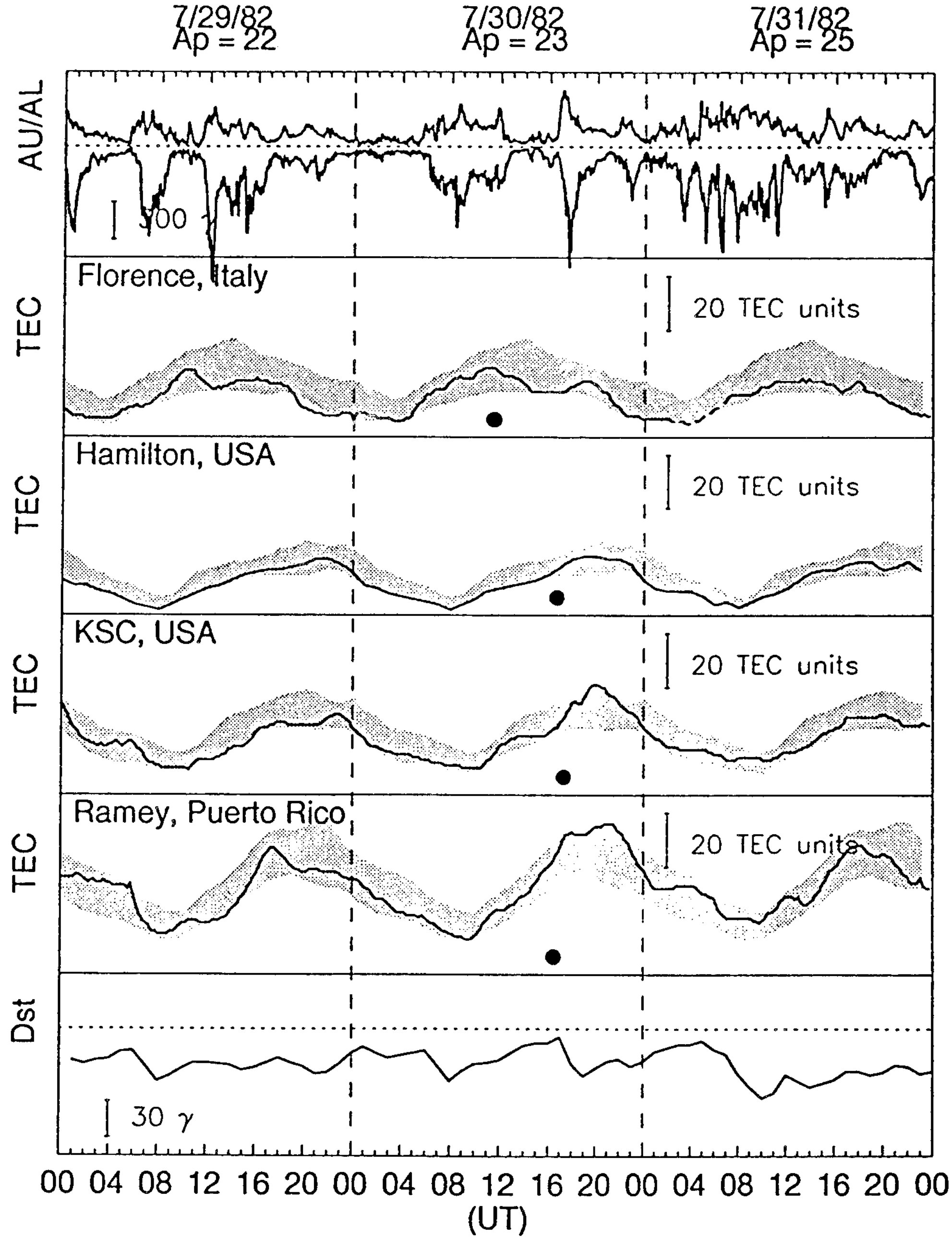
7/29/82
Ap = 22
7/30/82
Ap = 23
7/31/82
Ap = 25
AU/AL
100
TEC
Florence, Italy
20 TEC units
TEC
Hamilton, USA
20 TEC units
TEC
KSC, USA
20 TEC units
TEC
Ramey, Puerto Rico
20 TEC units
Dst
30 γ
00 04 08 12 16 20 00 04 08 12 16 20 00 04 08 12 16 20 00
(UT)

Figure 10

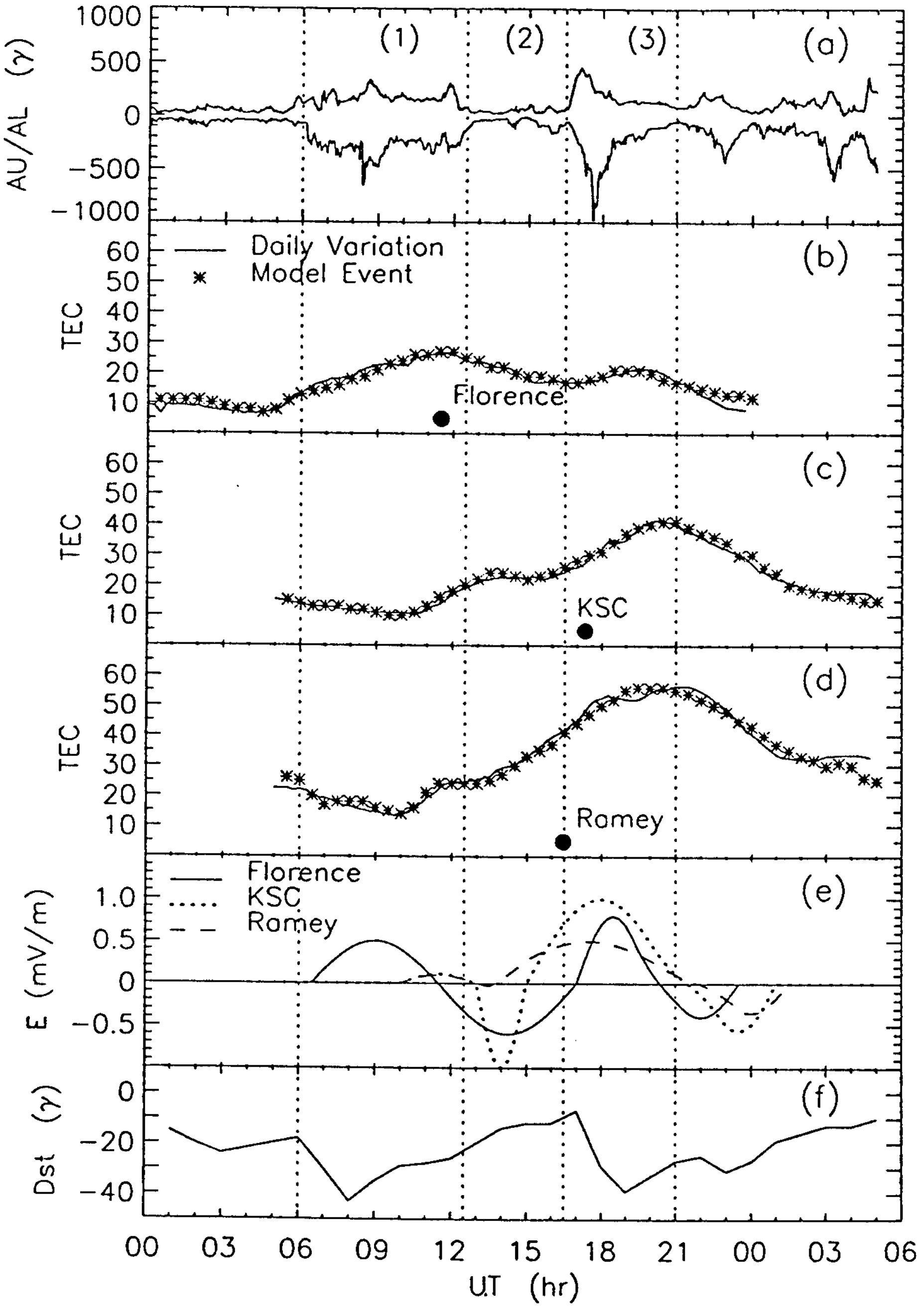

July 30, 1982.

Figure 11

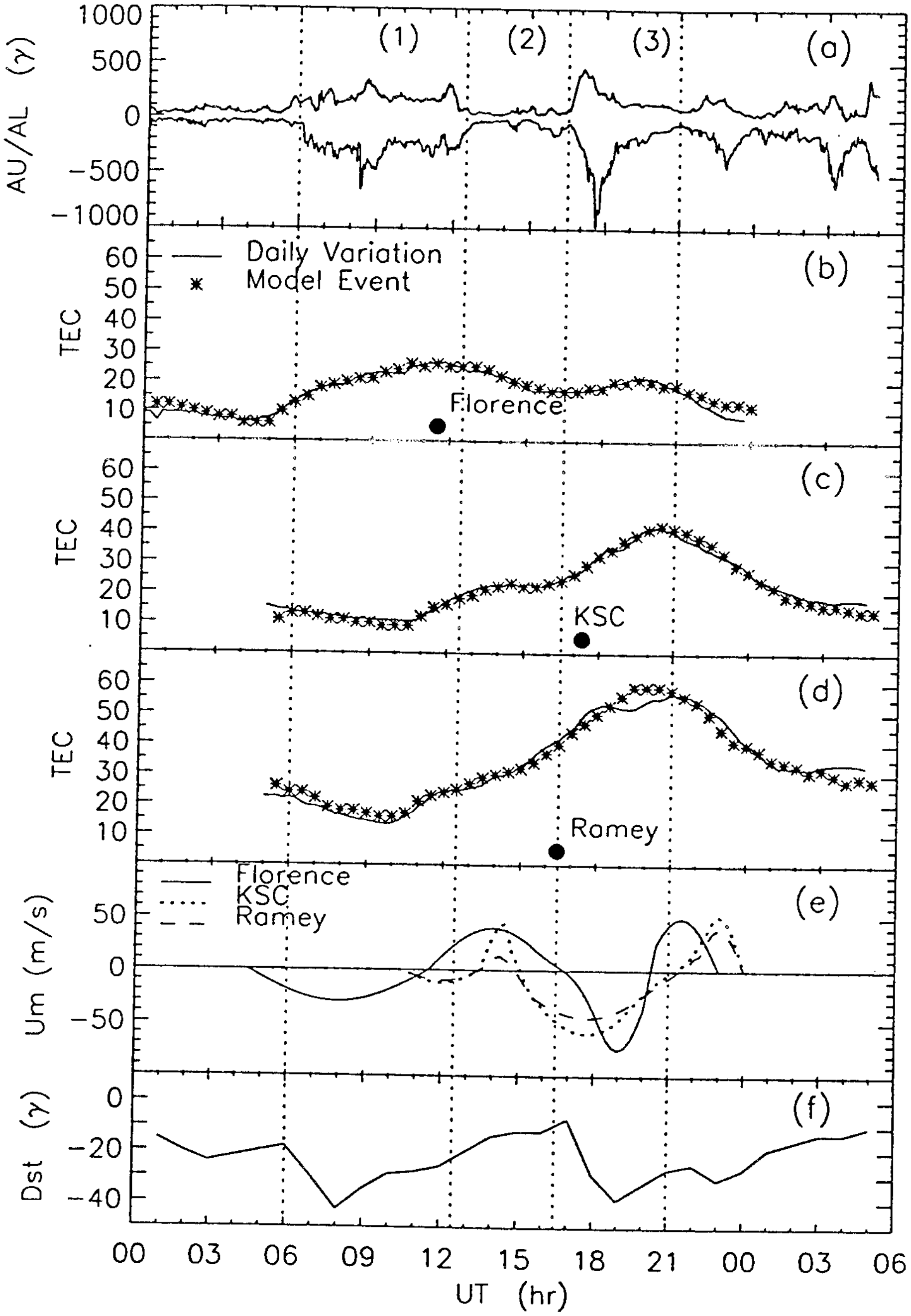

July 30, 1982.

Figure 12

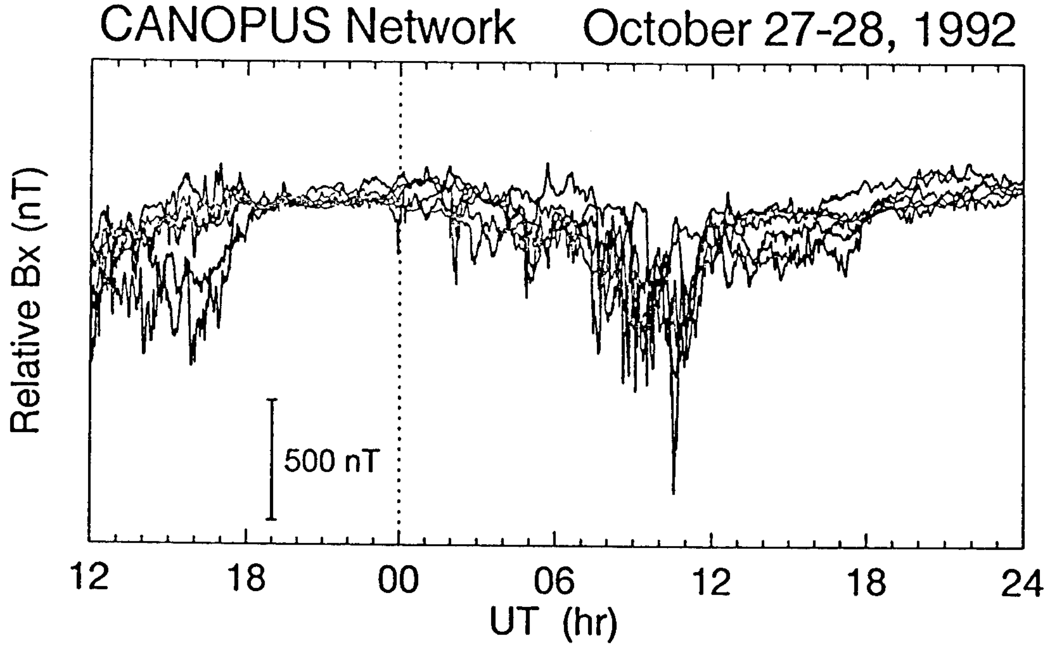
CANOPUS Network
October 27-28, 1992
Relative Bx (nT)
500 nT
12
18
00
06
12
18
24
UT (hr)

Figure 13

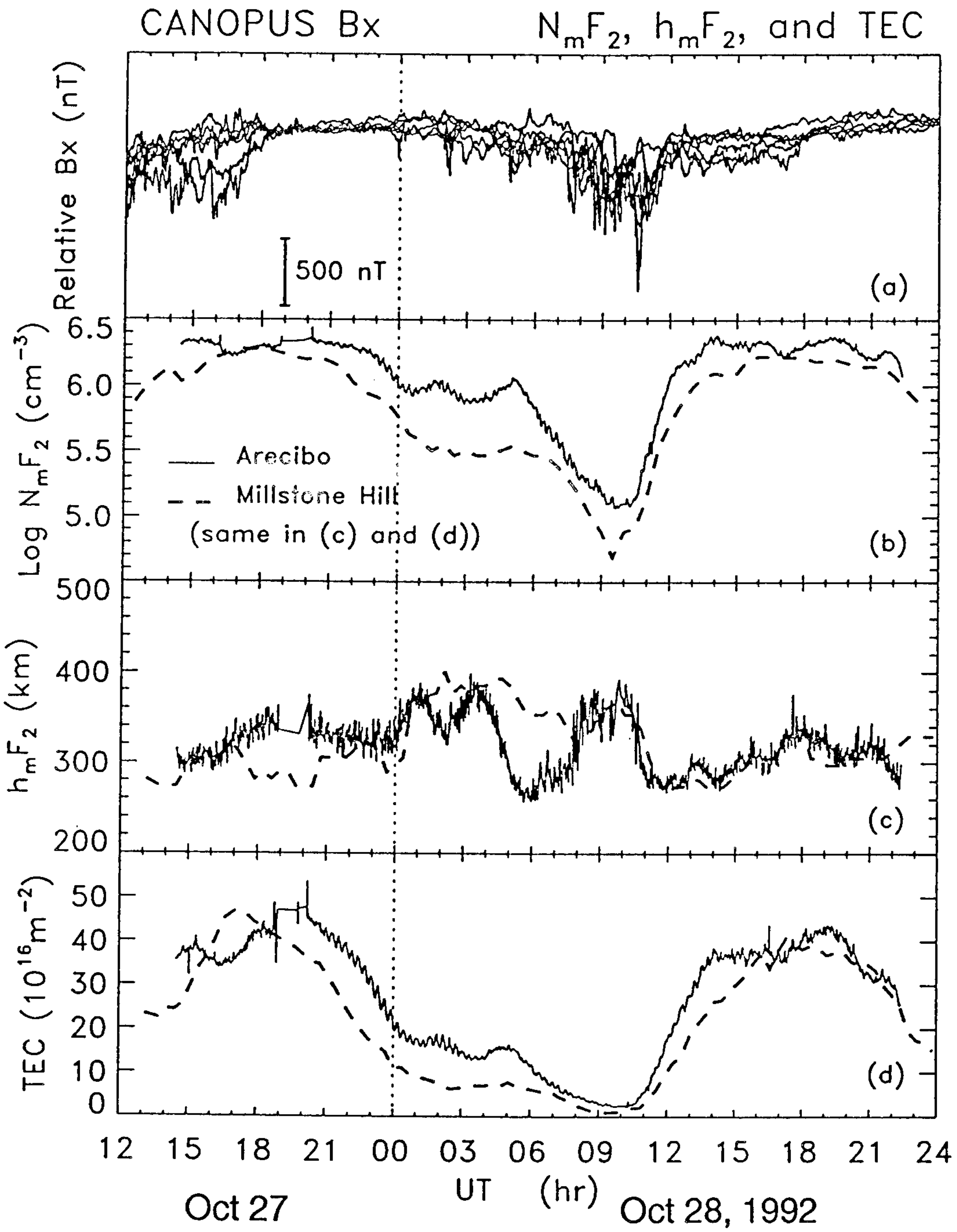
CANOPUS Bx
N_mF_2, h_mF_2, and TEC
Relative Bx (nT)
500 nT
(a)
Log N_mF_2 (cm^{-3})
6.5
6.0
5.5
5.0
Arecibo
Millstone Hill
(same in (c) and (d))
(b)
h_mF_2 (km)
500
400
300
200
(c)
TEC ($10^{16}m^{-2}$)
50
40
30
20
10
0
(d)
12
15
18
21
00
03
06
09
12
15
18
21
24
UT (hr)
Oct 27
Oct 28, 1992

Figure 14

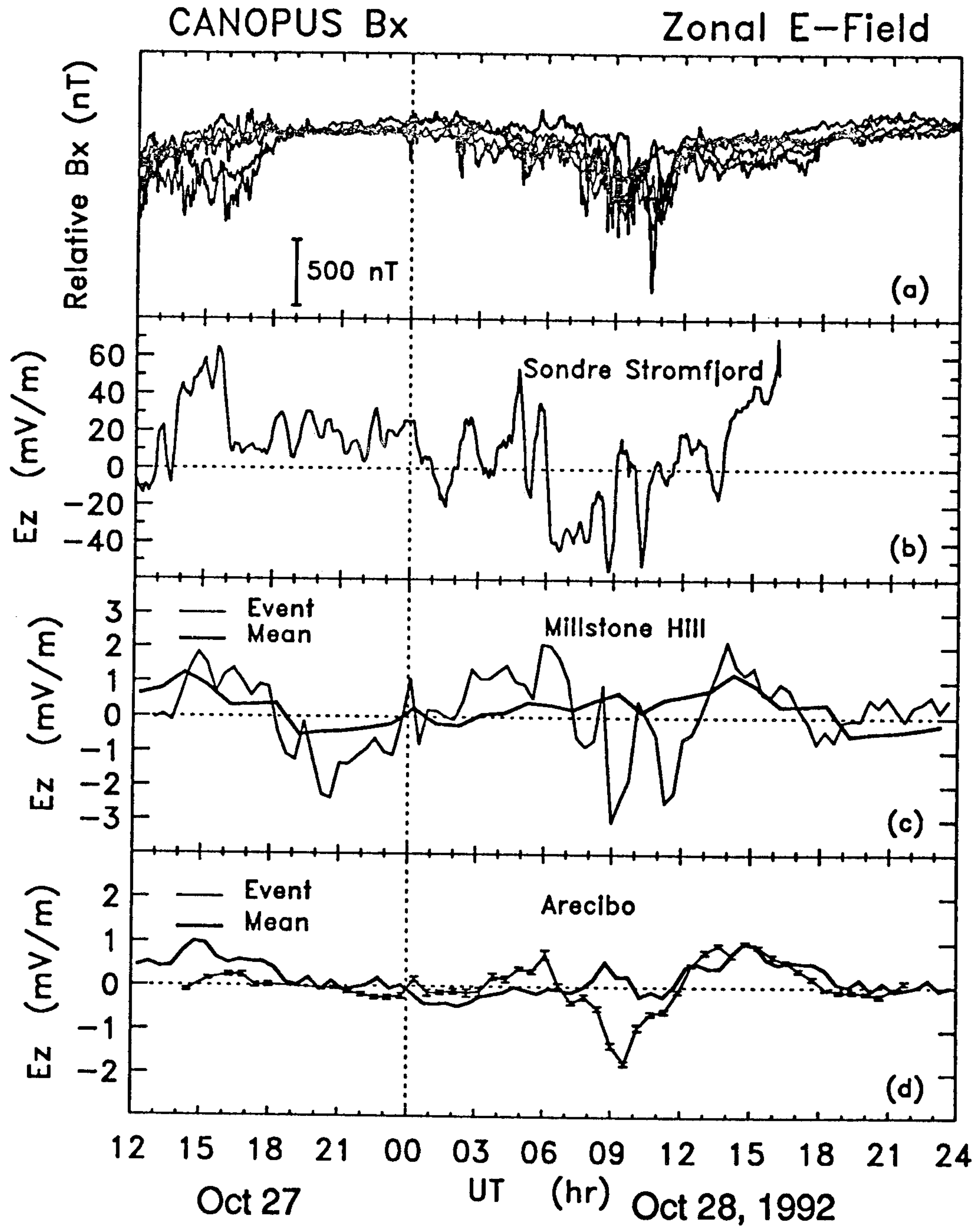

CANOPUS Bx
Zonal E-Field
Relative Bx (nT)
500 nT
(a)
Ez (mV/m)
60
40
20
0
−20
−40
Sondre Stromfjord
(b)
Ez (mV/m)
3
2
1
0
−1
−2
−3
Event
Mean
Millstone Hill
(c)
Ez (mV/m)
2
1
0
−1
−2
Event
Mean
Arecibo
(d)
12
15
18
21
00
03
06
09
12
15
18
21
24
Oct 27
UT (hr)
Oct 28, 1992

Figure 15.

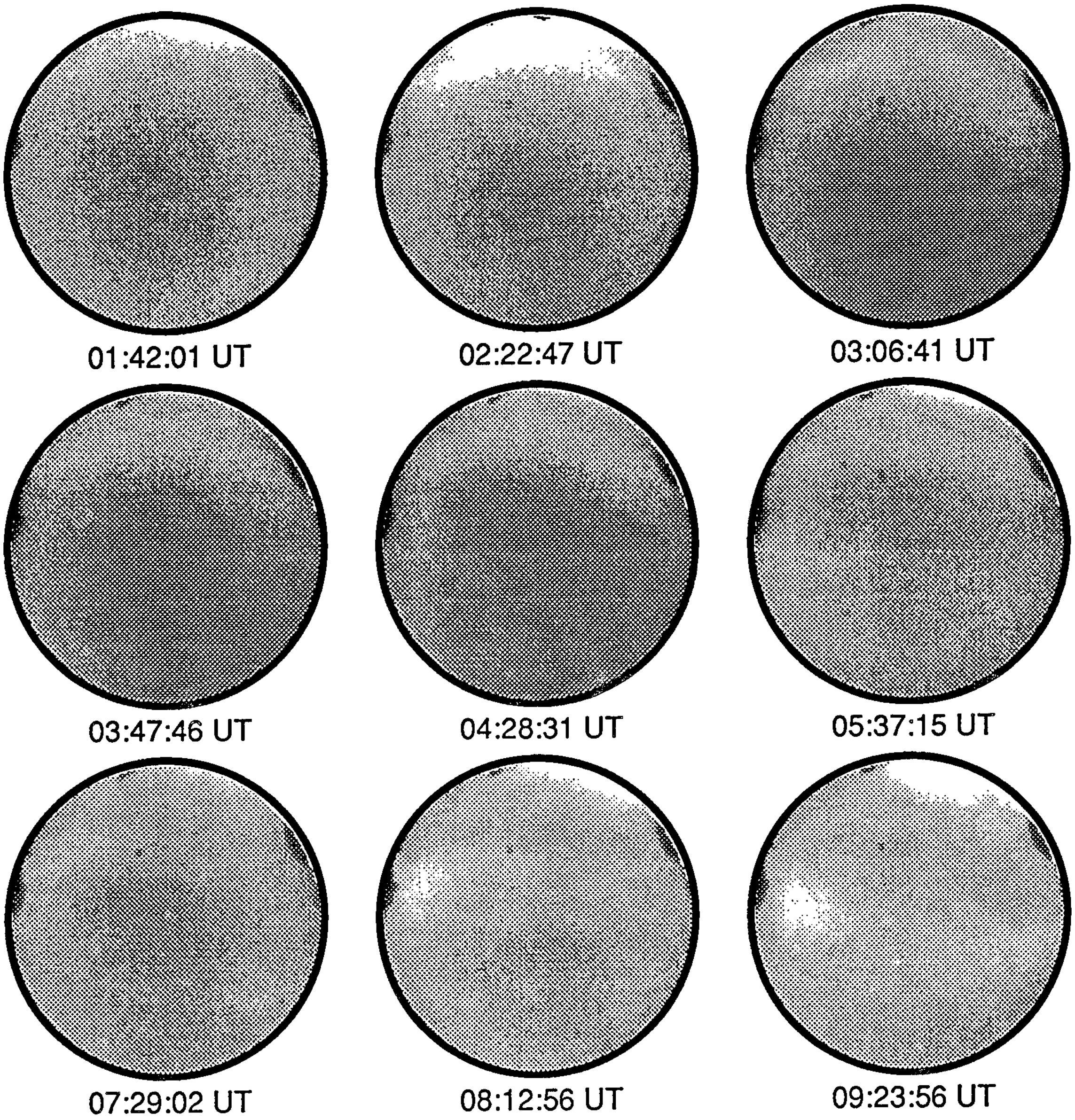

01:42:01 UT

02:22:47 UT

03:06:41 UT

03:47:46 UT

04:28:31 UT

05:37:15 UT

07:29:02 UT

08:12:56 UT

09:23:56 UT

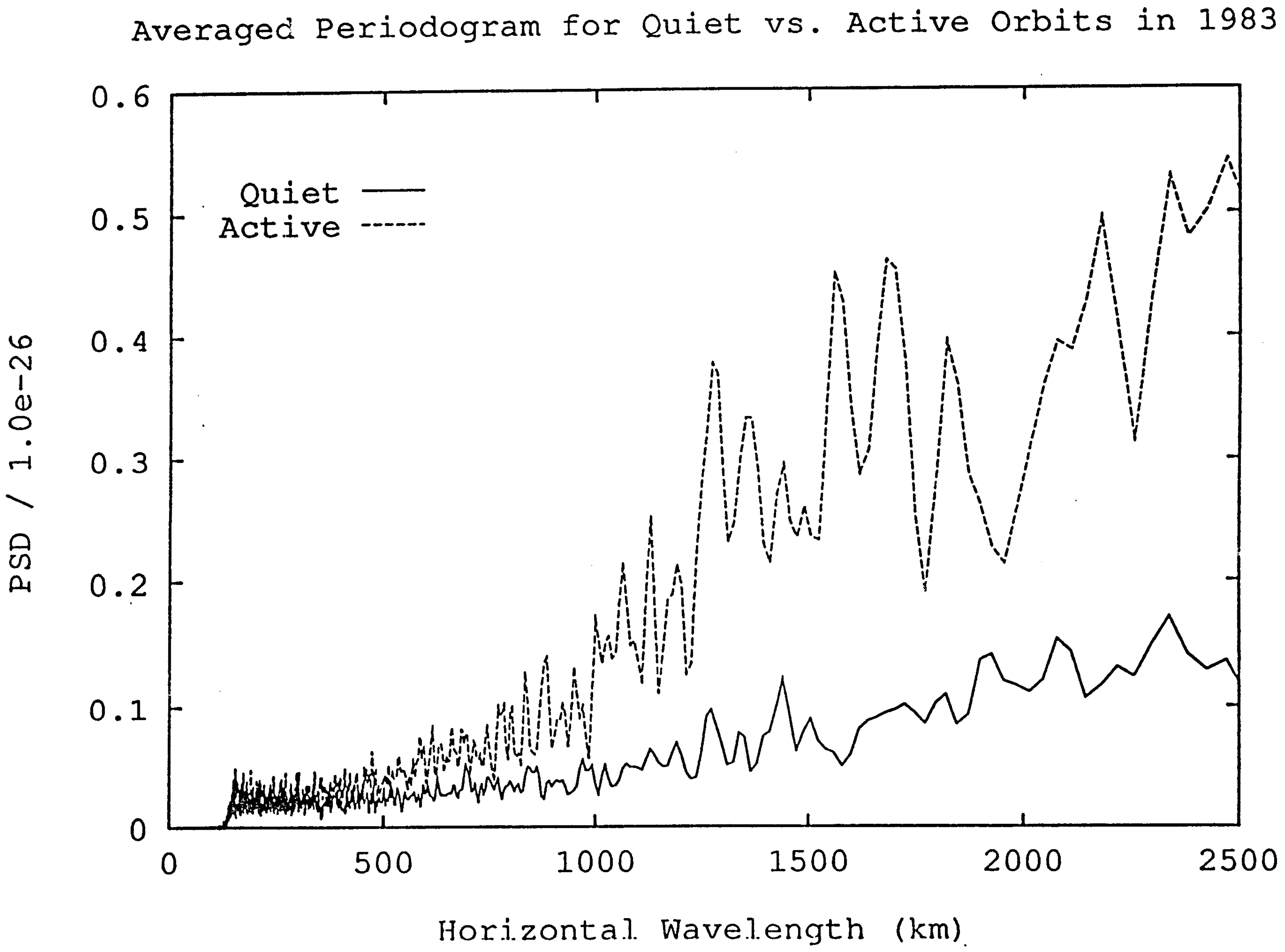
Averaged Periodogram for Quiet vs. Active Orbits in 1983
Quiet
Active
PSD / 1.0e-26
0.6
0.5
0.4
0.3
0.2
0.1
0
0
500
1000
1500
2000
2500
Horizontal Wavelength (km)

Figure 16

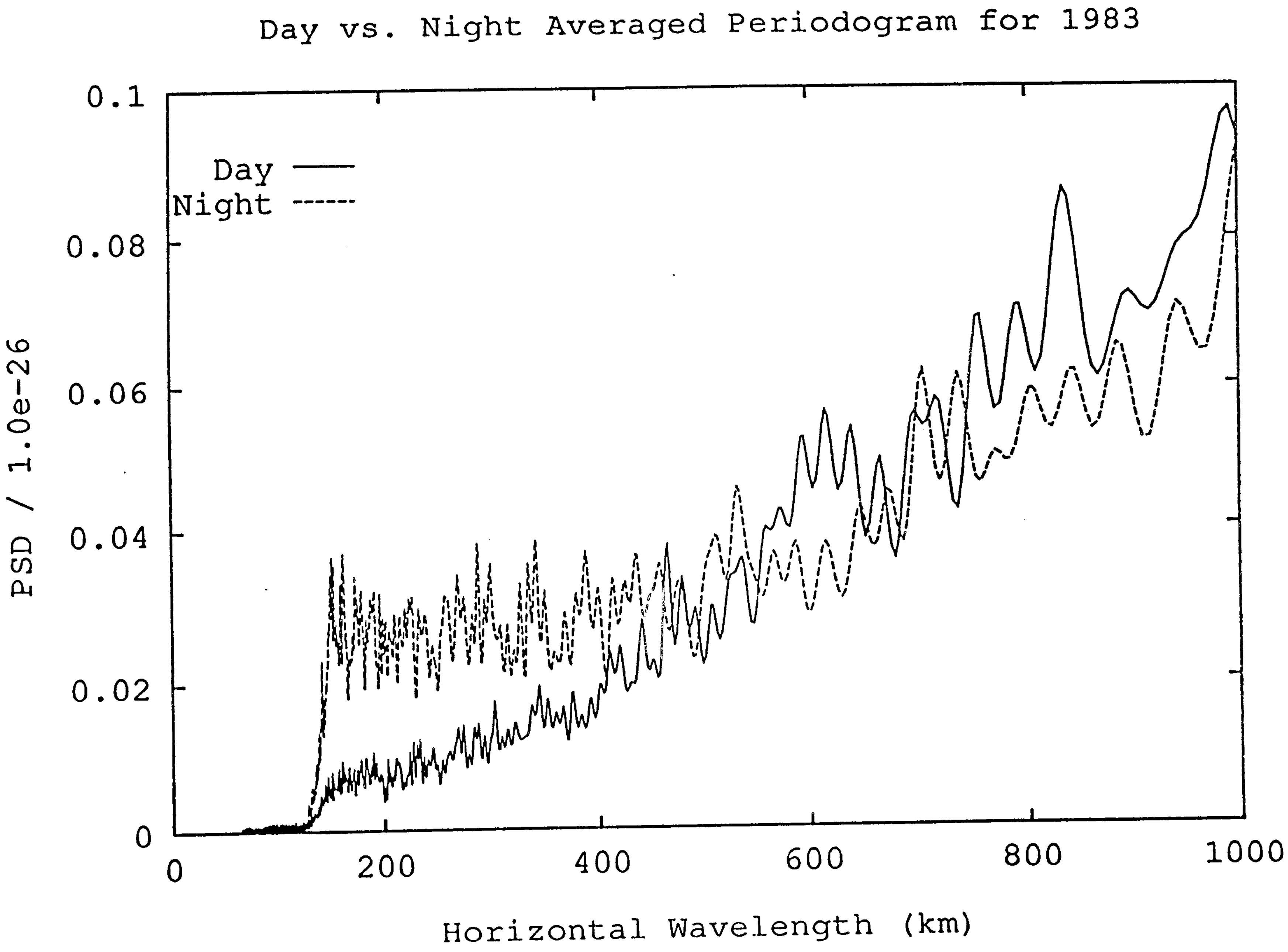
Day vs. Night Averaged Periodogram for 1983
Day
Night
0.1
0.08
0.06
0.04
0.02
0
0
200
400
600
800
1000
PSD / 1.0e-26
Horizontal Wavelength (km)

Figure 17

Figure 18.

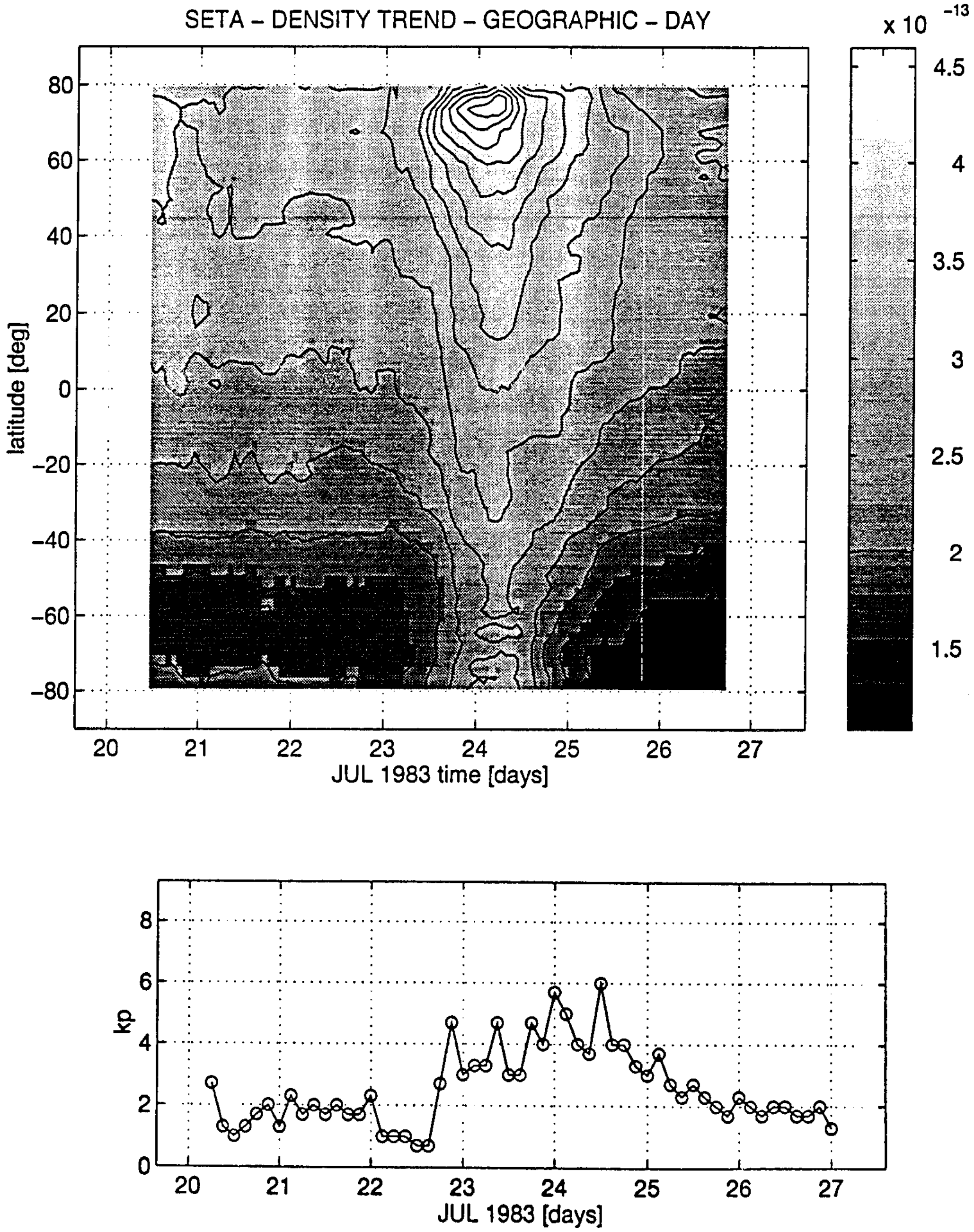

SETA – DENSITY TREND – GEOGRAPHIC – DAY
x 10 −13
4.5
4
3.5
3
2.5
2
1.5
latitude [deg]
80
60
40
20
0
−20
−40
−60
−80
20
21
22
23
24
25
26
27
JUL 1983 time [days]
kp
8
6
4
2
0
20
21
22
23
24
25
26
27
JUL 1983 [days]

Figure 19.

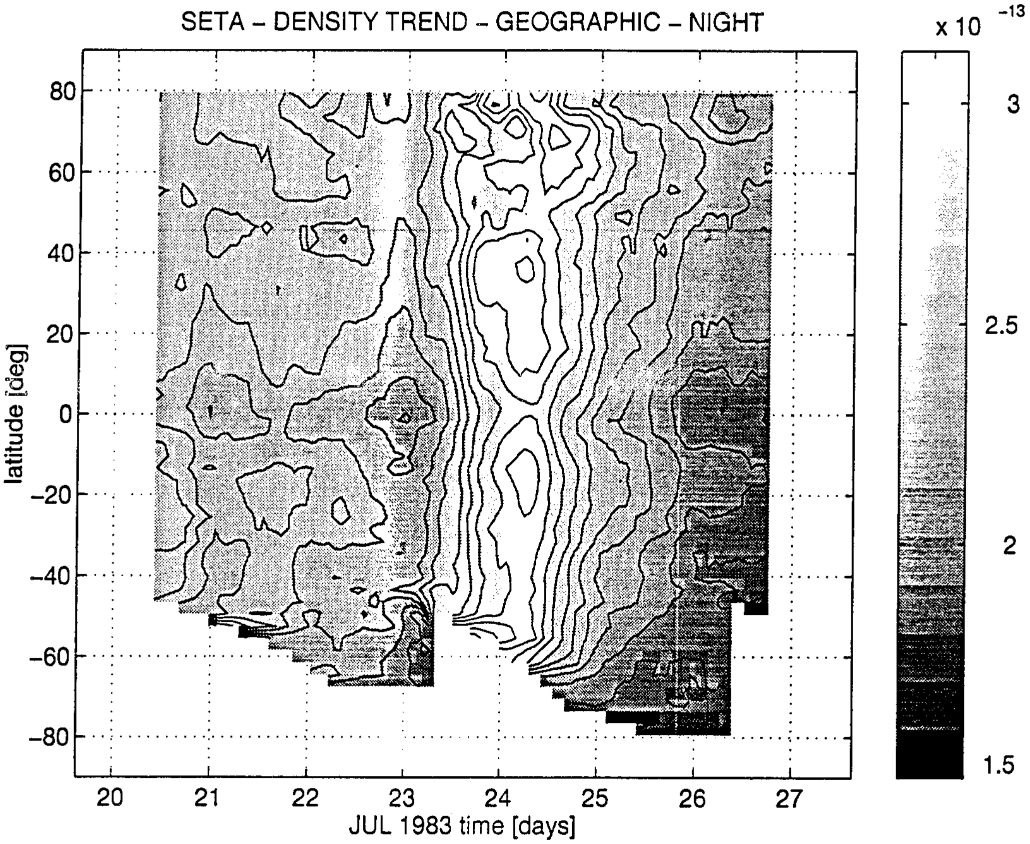
SETA – DENSITY TREND – GEOGRAPHIC – NIGHT
latitude [deg]
80
60
40
20
0
-20
-40
-60
-80
20
21
22
23
24
25
26
27
JUL 1983 time [days]
x 10 $^{-13}$
3
2.5
2
1.5

Figure 20.

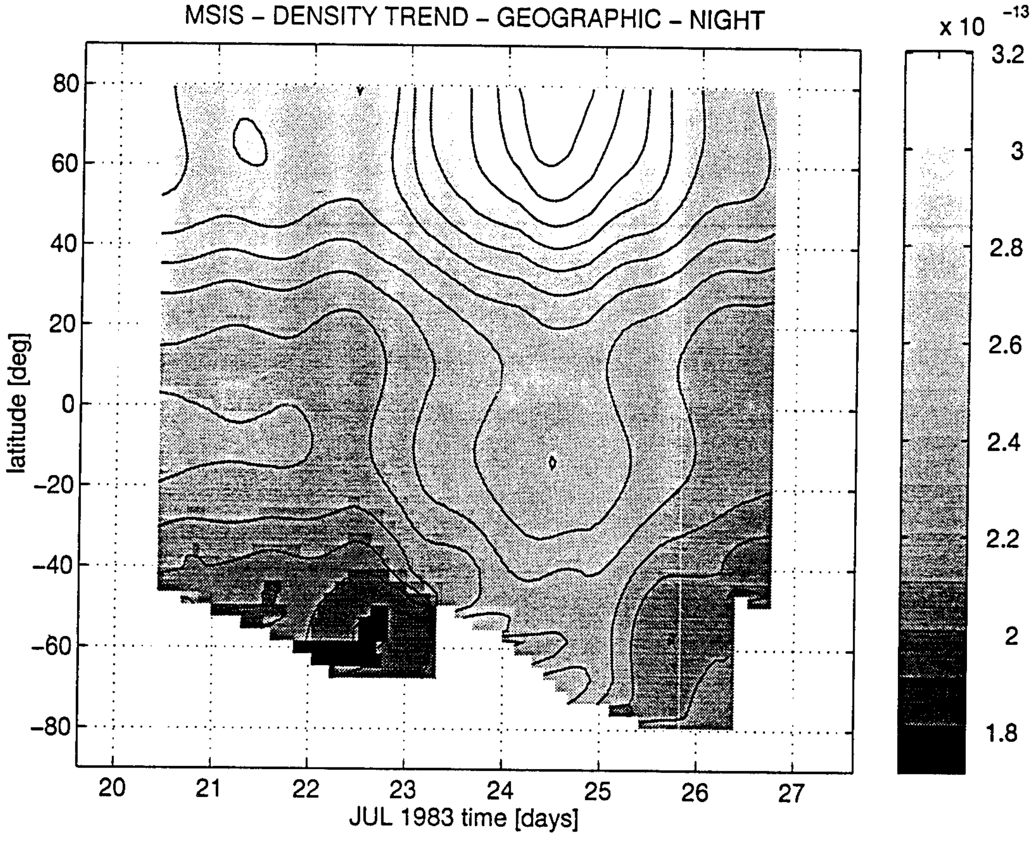

MSIS – DENSITY TREND – GEOGRAPHIC – NIGHT
latitude [deg]
80
60
40
20
0
-20
-40
-60
-80
20
21
22
23
24
25
26
27
JUL 1983 time [days]
x 10 $^{-13}$
3.2
3
2.8
2.6
2.4
2.2
2
1.8

Figure 21.

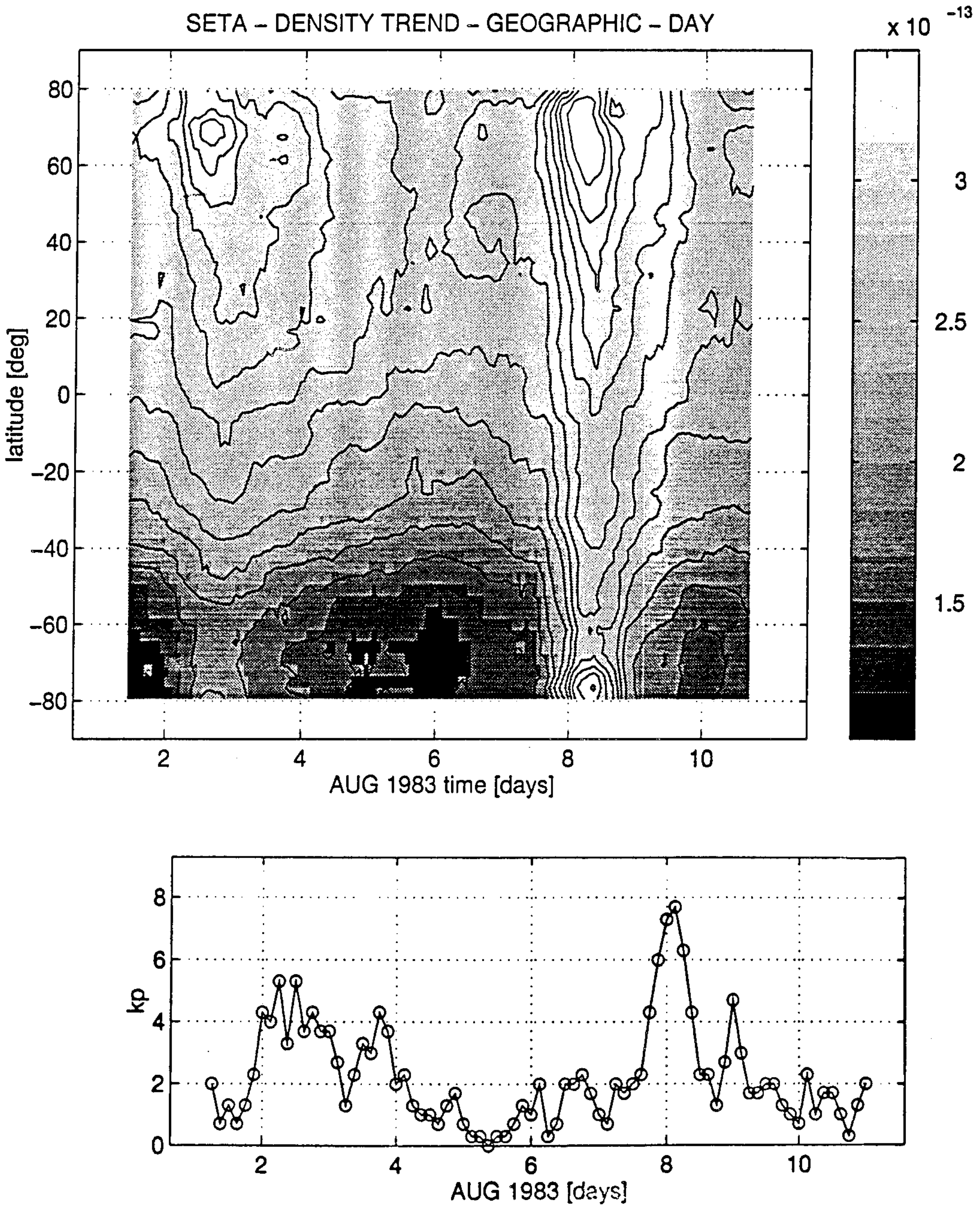
SETA - DENSITY TREND - GEOGRAPHIC - DAY
x 10 $^{-13}$
80
60
40
20
0
-20
-40
-60
-80
latitude [deg]
2
4
6
8
10
AUG 1983 time [days]
3
2.5
2
1.5
8
6
4
2
0
kp
2
4
6
8
10
AUG 1983 [days]

Figure 22.

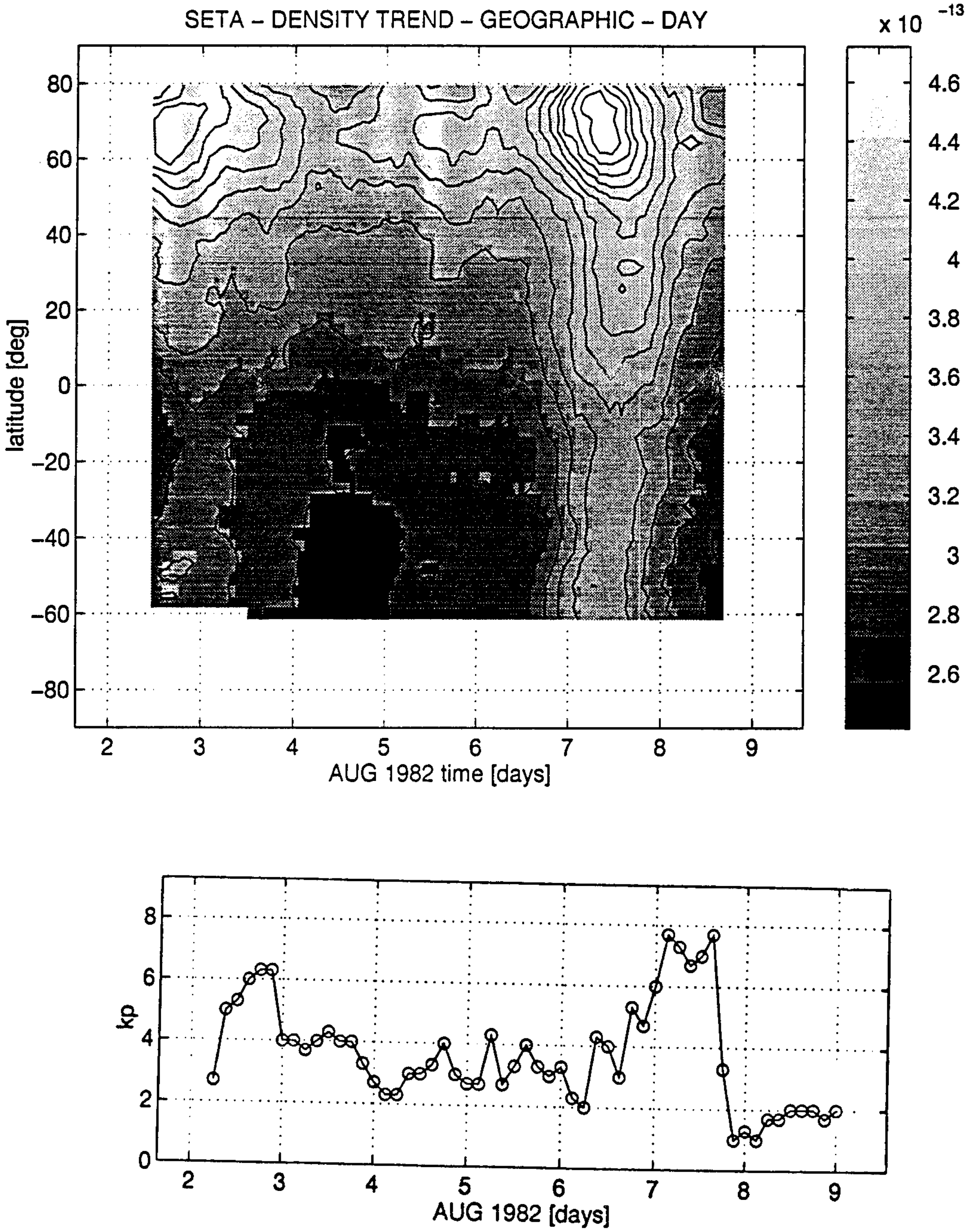
SETA – DENSITY TREND – GEOGRAPHIC – DAY
latitude [deg]
80
60
40
20
0
-20
-40
-60
-80
2
3
4
5
6
7
8
9
AUG 1982 time [days]
x 10 ⁻¹³
4.6
4.4
4.2
4
3.8
3.6
3.4
3.2
3
2.8
2.6
kp
8
6
4
2
0
AUG 1982 [days]

Figure 23.

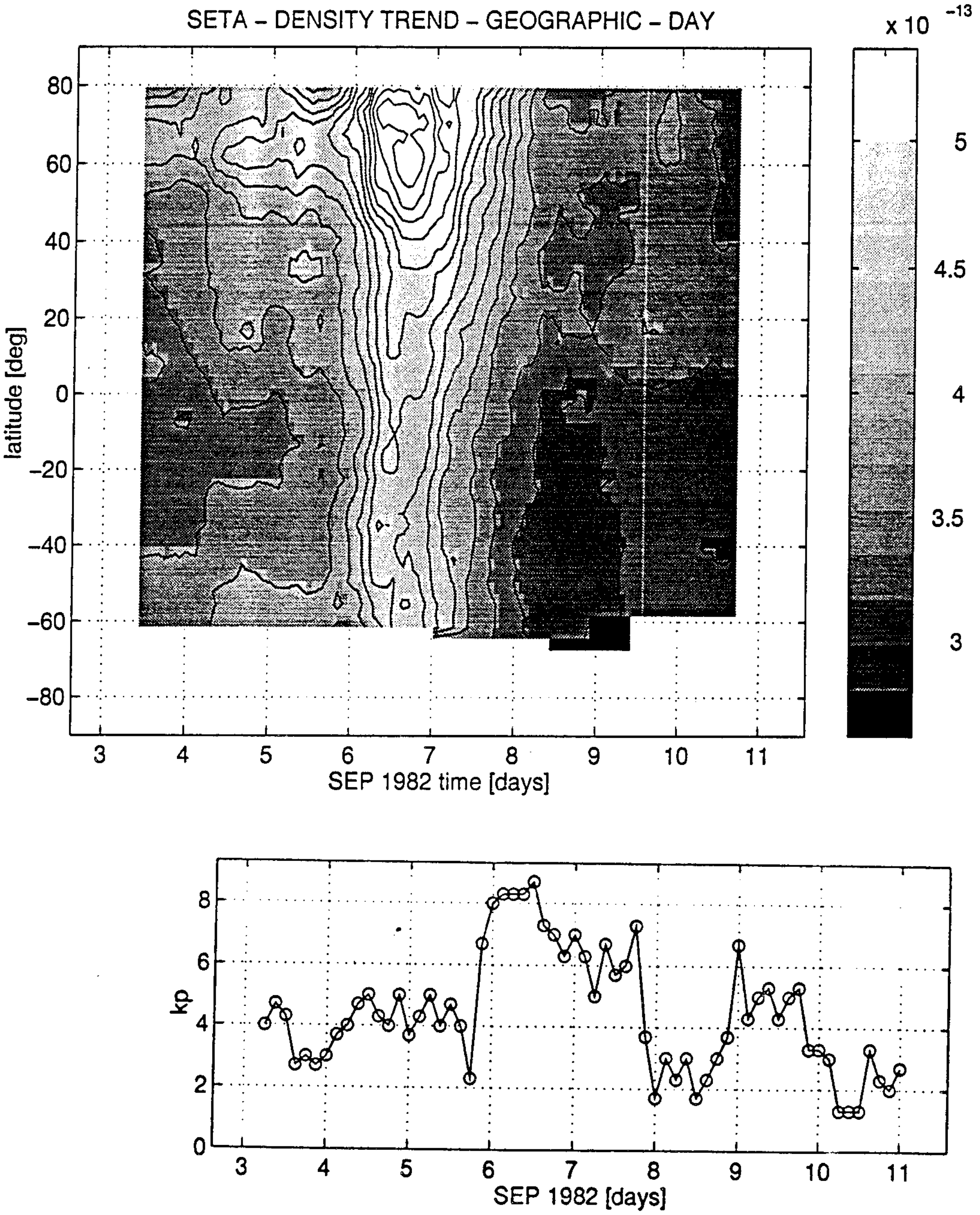
SETA – DENSITY TREND – GEOGRAPHIC – DAY
x 10 ⁻¹³
5
4.5
4
3.5
3
latitude [deg]
80
60
40
20
0
-20
-40
-60
-80
3
4
5
6
7
8
9
10
11
SEP 1982 time [days]
kp
8
6
4
2
0
3
4
5
6
7
8
9
10
11
SEP 1982 [days]

Figure 24.

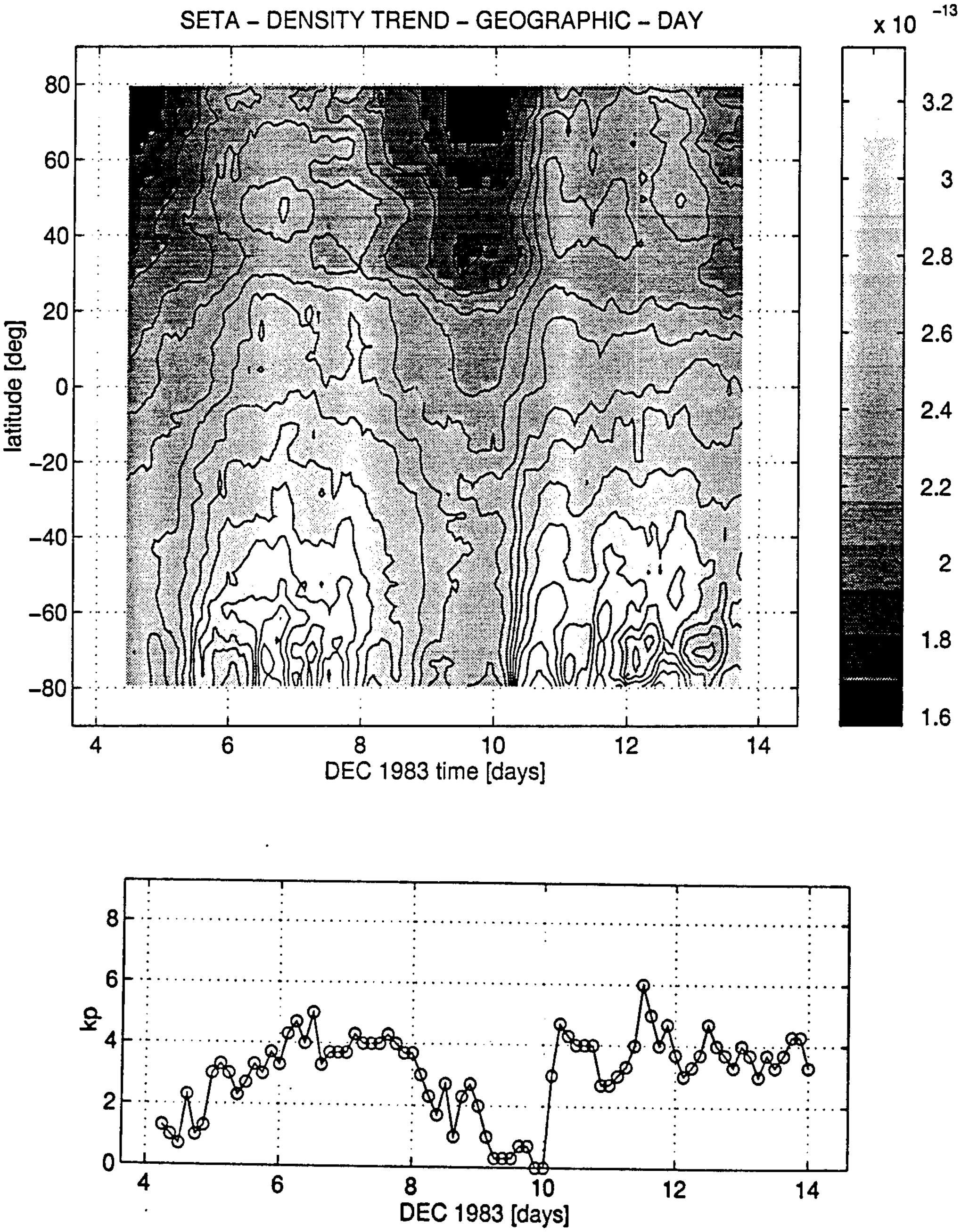
SETA - DENSITY TREND - GEOGRAPHIC - DAY
x 10 -13
latitude [deg]
80
60
40
20
0
-20
-40
-60
-80
4
6
8
10
12
14
DEC 1983 time [days]
3.2
3
2.8
2.6
2.4
2.2
2
1.8
1.6
kp
8
6
4
2
0
DEC 1983 [days]

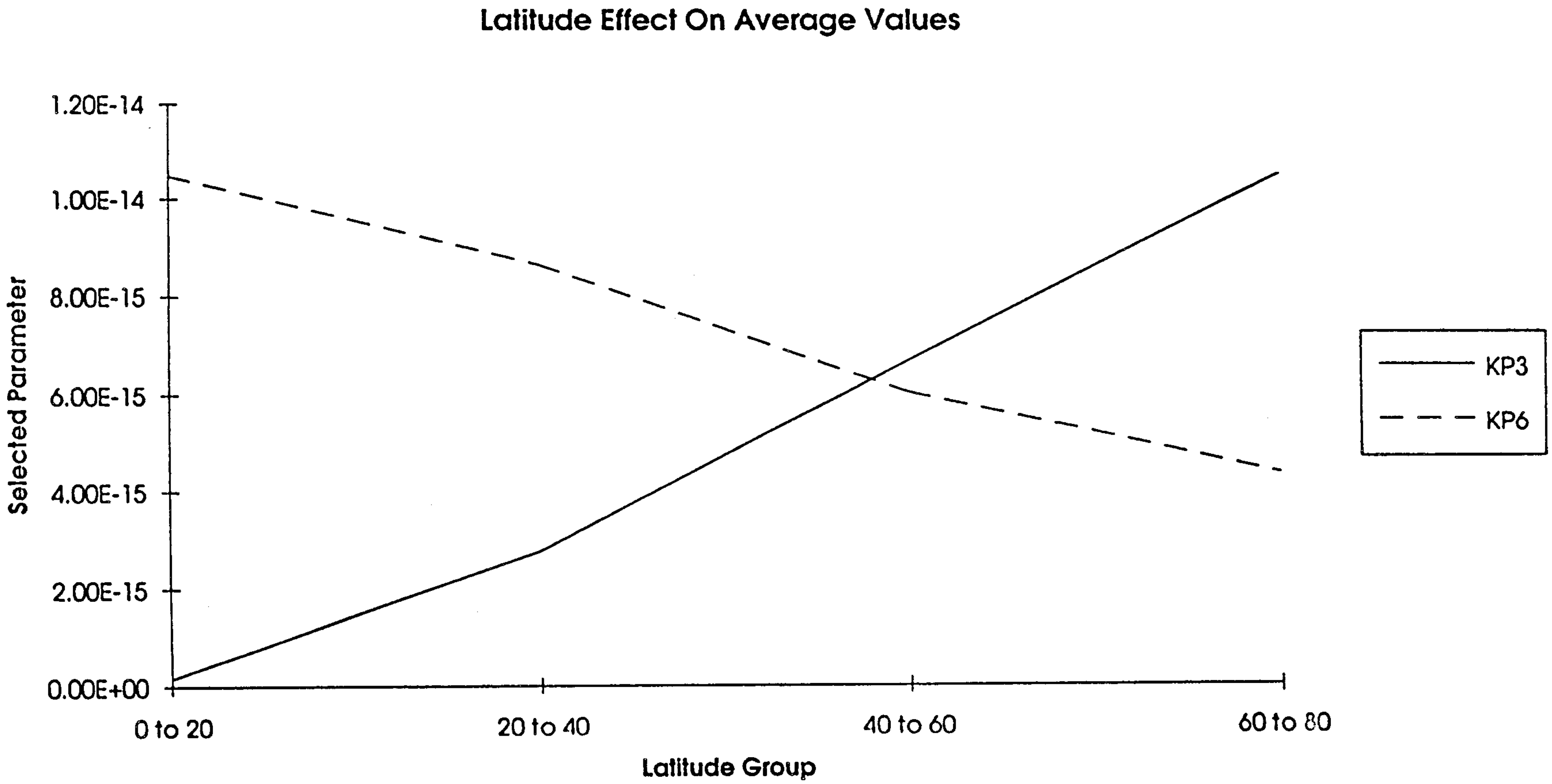
Latitude Effect On Average Values
Selected Parameter
1.20E-14
1.00E-14
8.00E-15
6.00E-15
4.00E-15
2.00E-15
0.00E+00
0 to 20
20 to 40
40 to 60
60 to 80
Latitude Group
KP3
KP6

Figure 25

Figure 26.

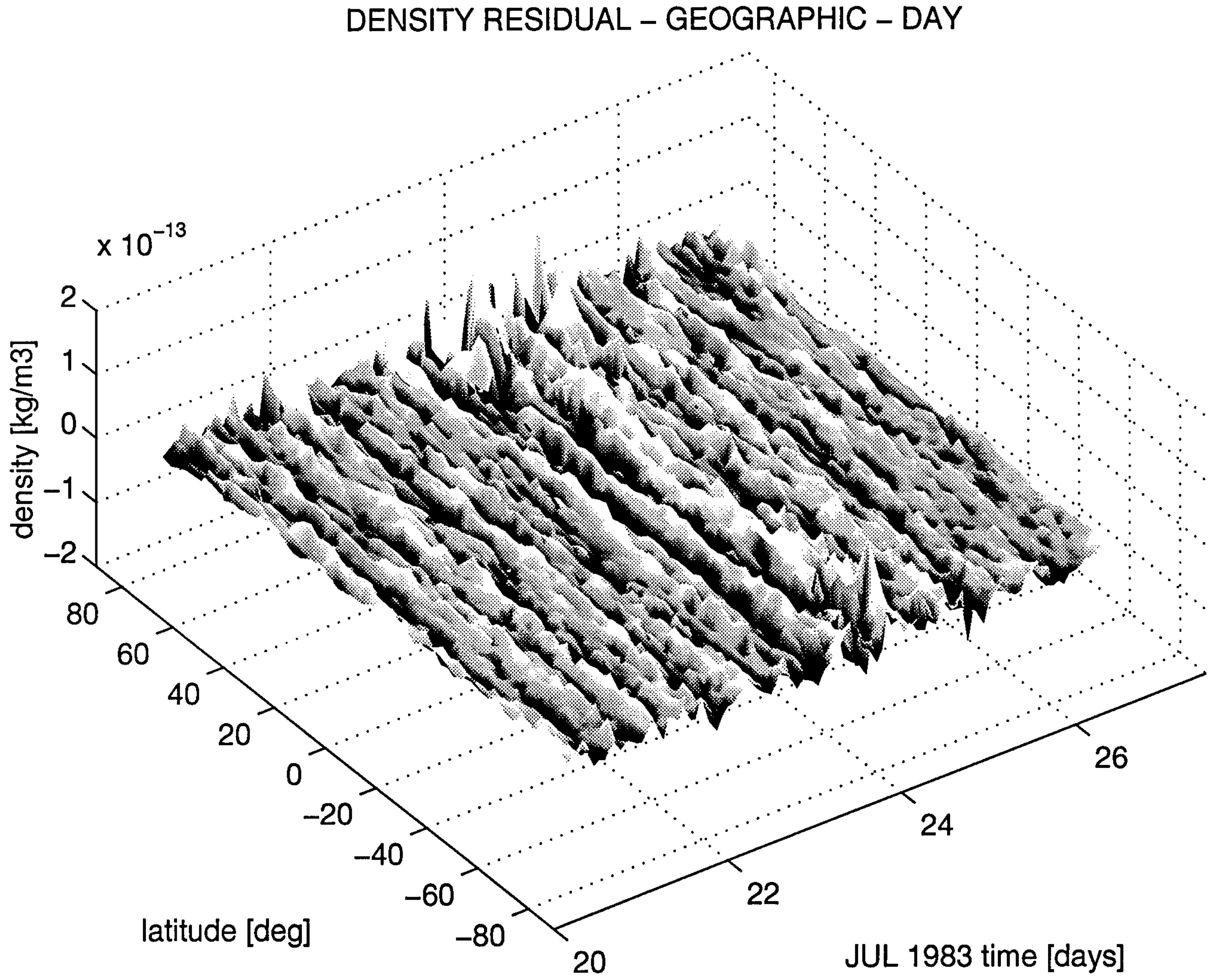
DENSITY RESIDUAL – GEOGRAPHIC – DAY
x 10^-13
2
1
0
–1
–2
density [kg/m3]
80
60
40
20
0
–20
–40
–60
–80
latitude [deg]
20
22
24
26
JUL 1983 time [days]

Figure 27.

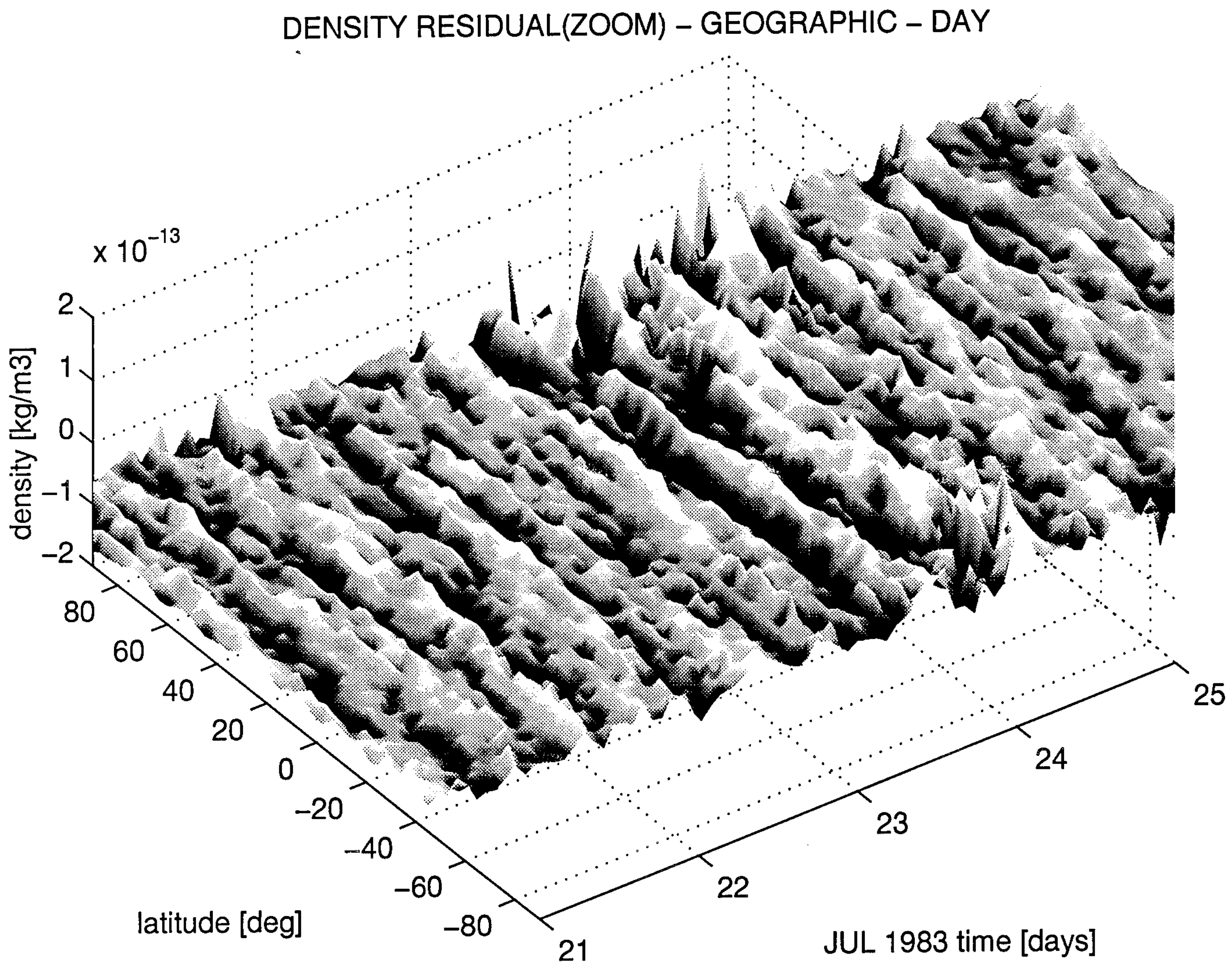
DENSITY RESIDUAL(ZOOM) – GEOGRAPHIC – DAY
x 10^-13
2
1
0
–1
–2
density [kg/m3]
80
60
40
20
0
–20
–40
–60
–80
latitude [deg]
21
22
23
24
25
JUL 1983 time [days]

Figure 28.

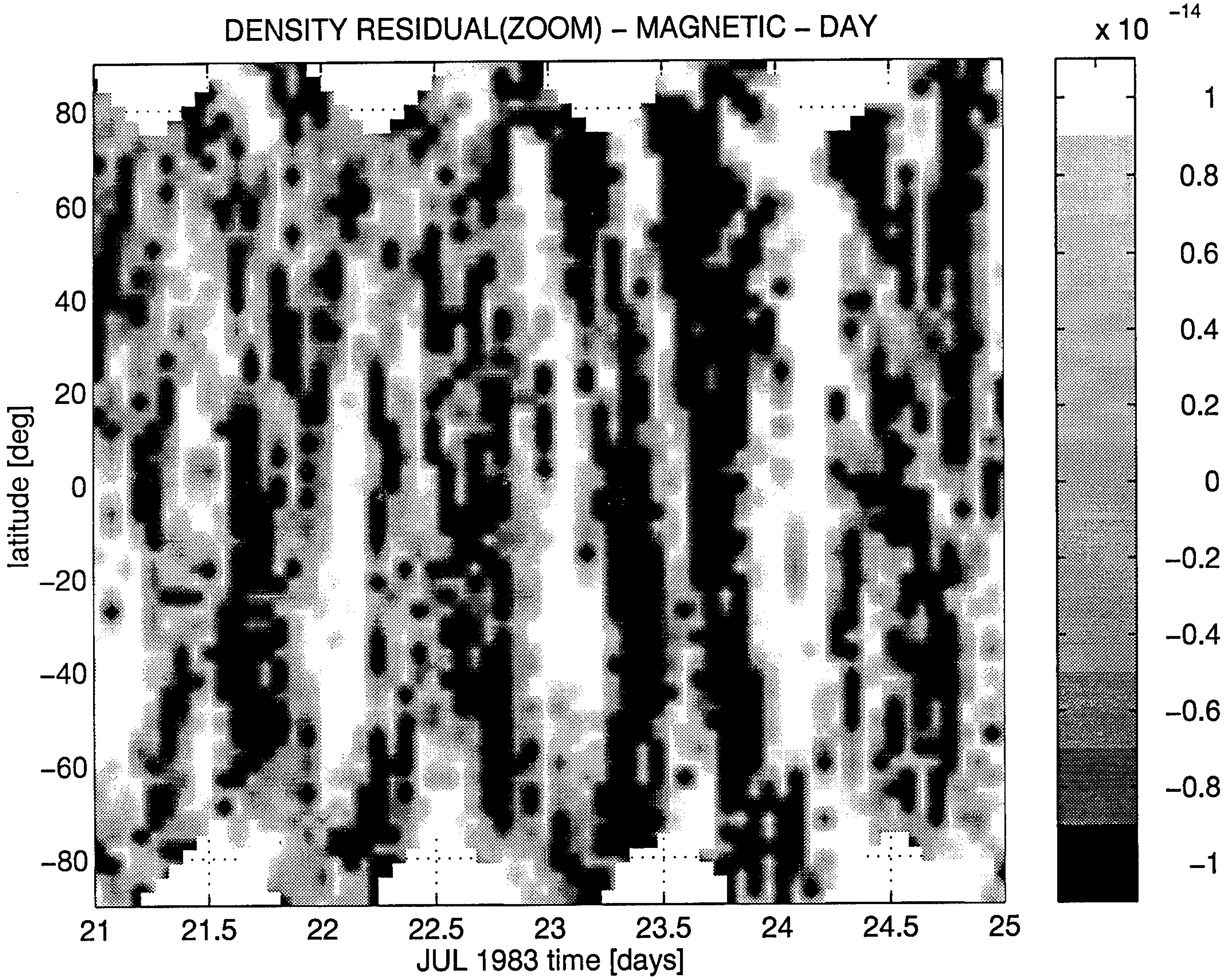
DENSITY RESIDUAL(ZOOM) - MAGNETIC - DAY
latitude [deg]
80
60
40
20
0
-20
-40
-60
-80
21
21.5
22
22.5
23
23.5
24
24.5
25
JUL 1983 time [days]
x 10^-14
1
0.8
0.6
0.4
0.2
0
-0.2
-0.4
-0.6
-0.8
-1